Core-shell Colloidal Quantum Dots For Photovoltaics With Improved Open Circuit Voltage

by

Yijin Guo

Submitted to the Department of Physics
in partial fulfillment of the requirements for the degree of

Bachelors of Arts

at

Mount Holyoke College

May 2020

Author .....
Department of Physics
May 8th, 2020

Certified by .....
Alexi C. Arango
Associate Professor of Physics
Thesis Supervisor

Accepted by .....
Alexi C. Arango
Chair, Department of Physics

Core-shell Colloidal Quantum Dots For Photovoltaics With Improved Open Circuit Voltage

by

Yijin Guo

Submitted to the Department of Physics
on May 8th, 2020, in partial fulfillment of the
requirements for the degree of
Bachelors of Arts

Abstract

Over the past decades, research efforts have been dedicated to solution processed photovoltaics based on colloidal quantum dots (CQD). Due to its tunable band-gaps, good stability in air and earth-abundant nature, lead sulfide (PbS) quantum dots have become competing materials for the production of low-cost flexible solar cells. Although the power conversion efficiency of CQD solar cell has increased rapidly in the past 10 years and reached certified efficiency of 16.6% in 2018, it is not comparable to silicon and perovskite solar cells with the power conversion efficiency of 27.6% and 25.2%.

One challenge that limits the performance of CQD solar cell is the incomplete absorption of the solar spectrum, resulting from the short diffusion length restricting the thickness of CQD layer to below 100 nm and could possibly solved by integrating multiple layers into a tandem structure. Another challenge is the open circuit circuit voltage (V_{oc}) and its deficit. High carrier recombination rates in PbS CQD photovoltaics can result in a reduction in V_{oc}. Surface states and sub-gap states are thought to increase recombination which leads to V_{oc} loss.

Here we present a method of forming an oxide shell on the CQD surface capped with native oleic acid ligands prior to the deposition of the CQD film and ligand swap. The core-shell QDs exhibit a narrowing in size distribution and the resulting devices yield improved V_{oc}. In addition, films of core-shell QDs are more resilient to damage incurred during sputter deposition of overlaying films. Because the thickness and uniformity of the oxide shell can be precisely controlled, a natural balance between trap passivation and charge transport can be achieved.

Thesis Supervisor: Alexi C. Arango
Title: Associate Professor of Physics

0.1 Acknowledgments

My first and foremost acknowledgement goes to my thesis supervisor and academic advisor, Professor Alexi C. Arango, for his continuous support and guidance through my four-year undergraduate experience at Mount Holyoke College. His enthusiasm and encouragement have affected me and shaped me into a researcher and a physicist.

I want to express my thanks to all previous alumni and present members of the Arango lab: Anne Bevin, Gillian L. Hagen, Ji-Won Ham, Hadley O'Malia and Maryann Valerio, for their dedication and efforts to our lab. I would like to thank Benjamin Zank's guidance and support during my very first semesters of researching, and Sue Shi, who had accompanied during the summer of 2018. Without all their mental and manual efforts my project would have never been possible.

I would also like to thank the entire Physics department of Mount Holyoke College, for their support and guidance throughout the four years. It is truly one of the most inspiring, encouraging and enlightening departments that I have seen.

Special thanks to Professor Katherine Aidala and Qiangfei Xia for their willingness of serving on my thesis committee, reading through and helping improving the quality of my thesis.

I am grateful to Professor Christine Aidala for providing me the opportunity to work in her lab during the summer of 2019, which enables me to experience a different lab experience at big universities. My thanks also goes to the Summer 2019 Aidala group, and especially Kara Mattioli for her guidance and help.

I am also thankful to all my friends from the Moho family, especially Renz Ren, Grace Xu, Louise Lu, Max Liu and Ye Zhang for their love and cheer. I would also like to thank my closest friends outside the Moho: Helen, Yunheng, Peipei, and Xincheng for their continuous love and support over the past ten years.

Finally, I would like to thank my family, especially my parents for their endless love and support, which crafted me into who I am: a confident and strong woman.

This work was supported by National Science Foundation EAGER Award # 1744671 and Mount Holyoke College Lynk Internship Funds.

Contents

List of Figures

List of Tables

Chapter 1

Motivation and Background

With increasing human development, the electricity use and energy demand have called worldwide attention. The drastically turning on demand of the electricity consumption from the upcoming consumers, per say the third world countries, could not be satisfied by limited fossil fuels, after decades of over-exploitation and extraction. Traditional fossil fuels not only produces unwanted byproducts like Carbon Monoxide (CO), Carbon Dioxide (CO_2) and Sulfur Dioxide(SO_2), but also results in global warming of 1.5 C above pre-industrial level; thus, substitutes of clean and inexhaustible energy source, such as sunlight, wind and tide, are desired. The potential of renewable solar resource on usable landing area well-matches the increasing future energy needs. In 2014, the International Energy Agency (IEA) envisions that under its high renewable scenario, by 2050 photovoltaics (PV) would contribute about 16% of the worldwide electricity consumption, and solar would be the world's largest source of electricity.

In this chapter, the historical perspectives and developments of photovoltaic will be introduced. The three main generations of PV technology will be introduced: silicon (Si) PV, including mono-crystalline Si, poly-crystalline Si and hybrid Si; thin-film PV, including amorphous Si, Cadmium Telluride (CdTe) and Copper Indium Gallium Diselenide(CIGS); and newly generated third-generation solar cells, including dye-sensitized, perovskite, organic and Colloidal Quantum Dot (CQD). The potential and advantages of CQD PVs will also be briefly discussed.

1.1 Historical development of photovoltaics

The rich history of human harvesting solar energy could be traced back to 7th century B.C, when magnifying glass was used to concentrate sun-rays to ignite woods. [16] The first solar collector was credit to Swiss scientist Horace de Saussure in 1767, in which glass and stuffed wool interlayer were used to trap solar heat. [17]

In 1839, the discovery of photovoltaic effect by French physicist Alexandre-Edmond Becquerel was marked as the milestone of photovoltaics. He successfully demonstrated a correlation between photon induced current and solar rays through an electrical-chemical setup with selective filters to distinguish heat and light, and varying color to generate a function of wavelength and current generated. The photo-conductivity of Selenium, also known as the increasing electrical conductivity with the introduction of electromagnetic radiation such as light, was firstly discovered in 1874 by English electrical engineer Willoughby Smith; three years later, William G. Adams and Richard E. Day verified the photoelectric effect in solid system by proving that light had caused a flow of electricity through solidified Selenium. The first solar cell was created in 1883 by American inventor Charles E. Fritts by coating Selenium with a sub-mm-thick thin gold layer, and a conversion efficiency of 1% - 2% was achieved, about $\frac{1}{20}$ of most modern photovoltaics.

Multiple patents were awarded to solar cell technology and solar storage techniques between 1880s and 1950s, including Edward Weston, Melvin Severy and Harry Reagon for 'solar cell' in 1887, 1894 and 1897 consecutively, Weston Bowser for 'solar storage' in 1899, Sven A. Berglund for 'methods of increasing the capacity of photosensitive cells' in 1914, Anthony H. Lamb for 'photoelectric device' in 1935, and Russel Ohl for 'light sensitive device' in 1941.

The first practical solar cell, with a conversion efficiency of 6%, about 6 times of the first cell, was created at Bell Laboratory by Gerald L. Pearson, Daryl M. Chapin and Calvin S. Fuller. Its structure was based on Si p-n junction. [18] The first push on the development of PV technology was from the U.S. government during 1950s to 1970s by funding the solar cells on space applications including communication

satellites and spacecrafts [19], although the price of solar electricity remained as high as $300 per watt in 1956 while a commercial power plant cost only 50 cents to build. While the efficiency level kept increasing and passed 14% in 1960 [16], significantly less costly PV was developed by using a poorer grade of silicon packaged with cheaper materials. The price was brought down to $20 per watt, which was more compatible with power lines. [20]

With the catalyst from the Arab oil embargo in 1973, further support from the U.S. government was committed to the development of PV technologies, which lead to the formation of The Solar Energy Research Institute (today the National Renewable Energy Laboratory NREL) [21], The Energy Research and Development Administration (ERDA) [22], and the Department of Energy (DOE). [23]

Based on leveled efficiencies and cost, photovoltaics could be categorized into three generations. Below, the three generations of solar cells will be discussed.

1.2 First generation solar cells: silicon

The most well-known traditional PVs are made from crystalline-Silicon (c-Si). It is still the most popular commercially used solar cells, possessing about 90% of residential-used solar cells. [24] [25] The c-Si PVs are of interests, since they provide consumers with a combination of the highest commercial efficiency and the longest lifetime, although there exists the risk of decreasing efficiency at higher temperatures.

Based on the type of Si used, there are four subdivisions of c-Si solar cells: mono-crystalline Si, poly-crystalline Si, and hybrid Si.

Each Si atom is bonded to neighboring atoms with four shared valence electrons, producing a well-defined band structure. [2] The arrangement of silicon atoms is shown in Figure 1-1 (a). As a type IV semiconducting material, Si could be doped with type III or V materials in the periodic table to introduce extra electrons and holes, producing extrinsic semiconductors. When doping with type V material like Phosphorous(P), a bonded Si atom is substituted with a P atom, which has five valence electrons available. Only four covalence electrons are shared by nearby Si

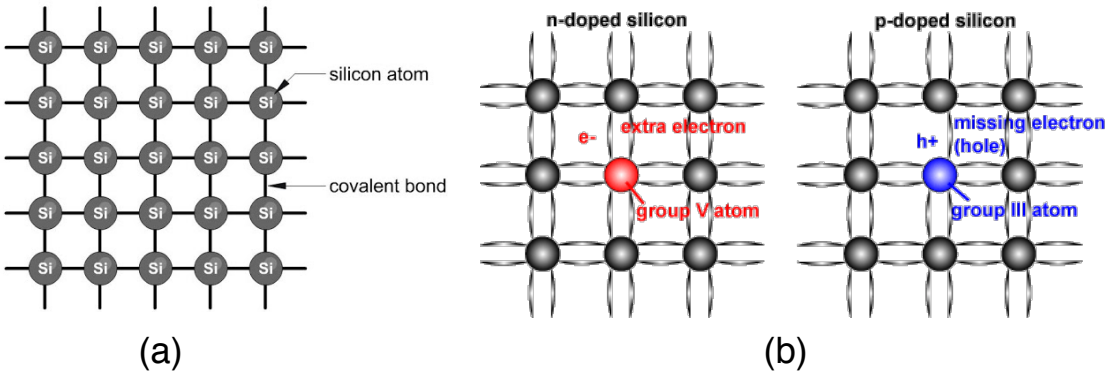

Figure 1-1: (a) Two-dimensional Si lattice. Figure from [1] (b) doping mechanism of Si. Figure from [2]

atoms, and thus there exists a free electron that could participate in conduction, producing n-type Si. P-type Si is produced the same way with type III materials like boron. The type V atom dedicates an extra hole to improve conductivity. [2] The doping mechanism of Si atoms is shown in Figure 1-1 (b).

Traditional c-Si PVs are composed of both p-type and n-type silicons. When n-type silicon are deposited onto p-type silicon base, they form a p-n junction. Electrons from n-type Si diffuses into p-Si and combines with holes, while holes in p-Si function the same way due to the diffusion mechanisms. An electric field is created because of the diffusion, as the lack of free electrons in n-type Si leaving excessive positive ions in it, and negative ions are left in p-type Si. When the number of recombined electron/hole pairs and the diffused electrons and holes reaches an equilibrium, there exists an area known as the depletion region, in which no free charge carriers are allowed to move. See Figure 1-2. As stated in the Photovoltaic Effect, when sun-lights are incident on the p-n junction solar cell, the energetic photons with suitable wavelength would transfer energy to electrons and enable the electrons to jump from the valence band to conduction band. Once been excited to the conduction band, the previously trapped electrons are free to move through the p-type Si and enter the n-Si driven by the built-in electric field in the depletion region. Since the back electrode of the solar cell is connected to the front electrode, electrons are free to travel to p-Si through the chord, combining with holes in it, producing electricity and driving the

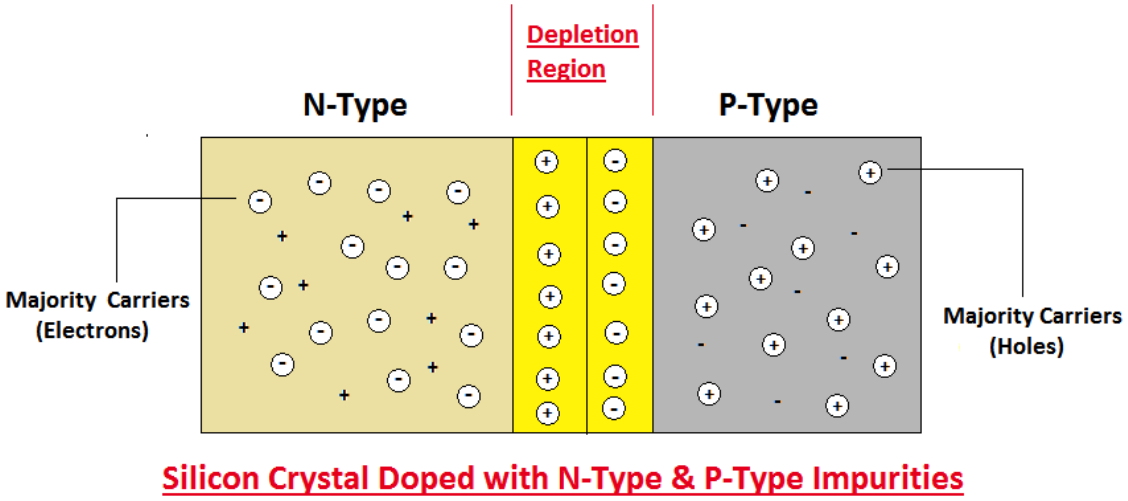

Figure 1-2: p-n juntion. Figure from [3].

load. Figure 1-3 shows the construction and function diagram of traditional c-Si p-n junction solar cells.

1.2.1 Mono-crystalline silicon cells

Often been called single-crystal Si, the mono-crystalline Silicon is made of an unbroken, continuous chain of crystal lattice. It is grown from a slow and expensive production process, usually the Czochralski method, which is performed in an inert atmosphere and crucible to avoid impurities.

As the first-generation PVs, in which early modules been constructed in the 1970s, single-Si solar panels are still dominant in the market, representing their durability and longevity. Most single-Si solar panels are guaranteed for 25-year warranty. [26] As mentioned earlier, they are also known for highest conversion efficiency. Compared with the thin film solar panels, which are made of toxic or accumulative materials like CdTe, single-Si PVs use the second most abundant element in the Earth's crust and are much less hazardous to the environment.

However, due to the high purity required for the initial material, the single-Si wafer is usually grown via the Czochralski process, and therefore the initial cost for producing single-Si photovoltaics is dramatically high. The costly transportation of

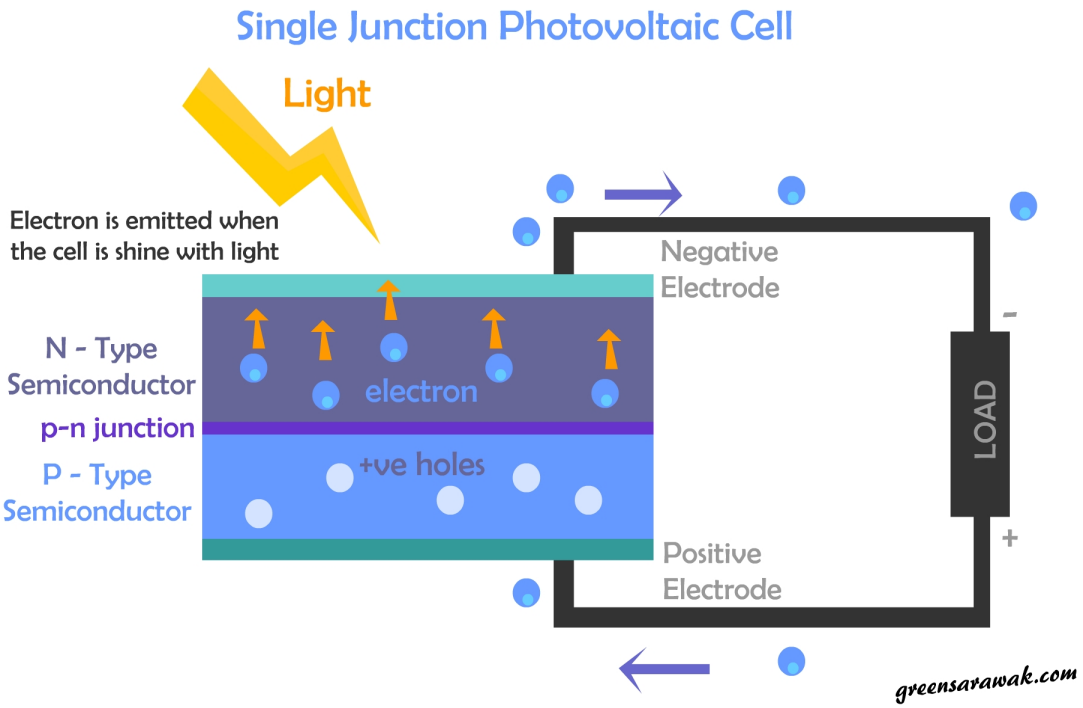

Figure 1-3: Construction diagram consisting of p-n junction c-Si solar cell. Figure from [4].

fragile, bulky single-Si solar panels is also problematic, leaving spaces for further improvement.

1.2.2 Poly-crystalline silicon cells

Poly-crystalline Si (poly-Si) are composed of small silicon crystals. While poly-Si could be produced with ultra purity (over 99.99%), the production cost is significantly lower than that of c-Si wafer, as the growth condition are not required to be tightly controlled. However, due to the presence of grain boundaries in poly-Si, the material parameters are much lower than c-Si and thus introducing excessive defect energy levels into the bandgap, increasing the recombination and therefore reducing the conversion efficiency. While c-Si wafers exhibit homogeneous feature and appear to be dark blue, poly-Si could be distinguished by its metal flake effect. See Figure 1-4 for mono-crystalline and poly-crystalline silicon solar cells. Efforts have been made to improve the power conversion efficiency and catch that of c-Si panels. Recently, Trina Solar has reported a PCE of 23.2% with poly-Si cells, about 86% of the recorded PCE of 27.6% for c-Si cells.

1.2.3 Hybrid silicon

Recently, hybrid solar cells have been reported based on silicon and compound semiconductor materials, with best recorded efficiency of 31.1%. [27]

1.3 Second generation solar cells: thin film

Thin film solar cell is considered as the second generation PVs, made from depositing thin layers of materials on back substrate, with thicknesses varying from nanometers to tens of micrometers, about 20 times thinner of conventional solar panels made from c-Si wafers. Its ultra-thin nature guarantees the thin-film solar cells to be light-weighted and flexible, which enables them to be exceptionally suitable for installations on roofs and semi-transparent windows. See Figure 1-5

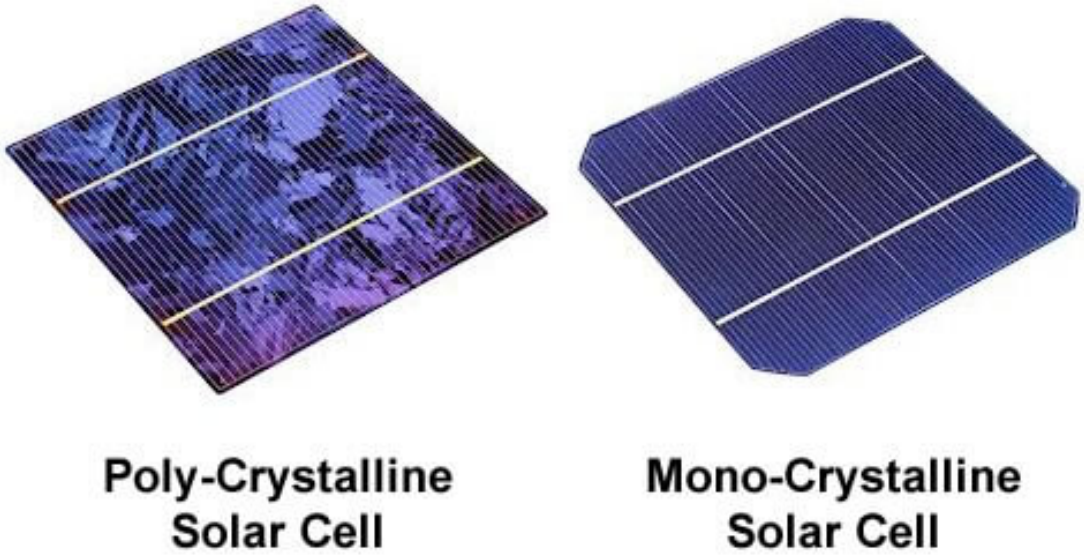

Figure 1-4: c-Si and poly-Si solar cells. Figure from [5].

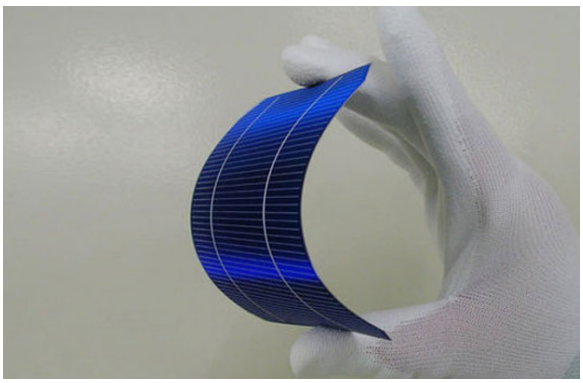

Figure 1-5: Thin-film solar PVs. Figure from [6].

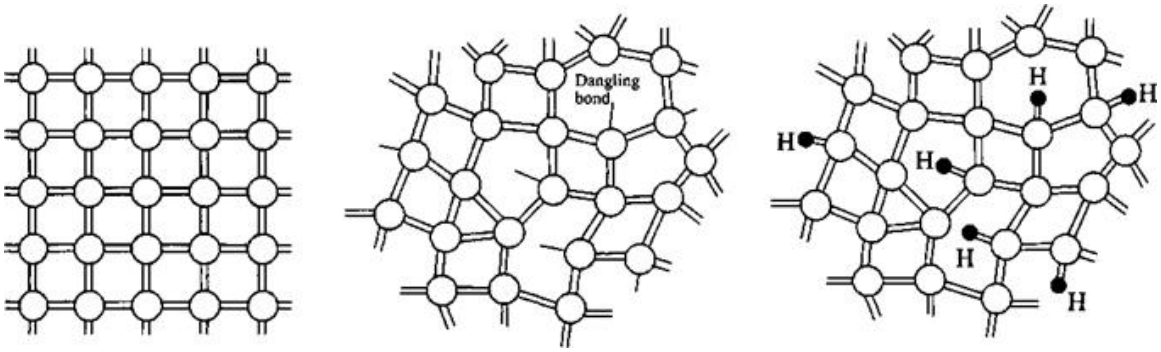

Figure 1-6: Crystalline and amorphous silicon. Figure from [7].

Because of less material used for production and less precise fabrication conditions, the thin-film solar cell could be manufactured at much lower cost, with the sacrifice of power conversion efficiency. The highest recorded lab efficiency of thin-film PVs reaches 23.4%. It also experiences faster degradation in accelerated life testing under laboratory condition. [28]

Commercially used thin-film PVs include Cadmium Telluride (CdTe), Copper Indium Gallium Diselenide (CIGS), and amorphous silicon.

1.3.1 Amorphous silicon cells

While single- and multi-polycrystalline Si exhibit a long range ordered crystal lattice, the amorphous silicon (a-Si) shows a disordered nature with dangling bonds and floating bonds, which results in low mobility and hence hinders device performances. Excessive hydrogen atoms are introduce during the fabrication of a-Si to lower the defect density and to improve conductivity. See Figure 1-6 for the structure diagram of a-Si. When manufacturing, thin layers of a-Si are deposited onto flexible substrate made of metal, glass or plastic. Although the production cost is relatively cheap, compared with that of c-Si solar cell, a-Si PVs struggle to compete with conventional crystalline Si PVs due to its low device performance and has been used only on devices that require low power, like calculators.

1.3.2 CdTe and CIGS cells

Cadmium Telluride (CdTe) and Copper Indium Gallium Diselenide (CIGS) are popular materials for producing second-generation thin-film solar cells, possessing about 16.8% of the photovoltaics industry. The best recorded laboratory efficiency of CdTe solar cell has reached at 22.1% at 2019 [6]. The low-cost manufacturing advantage and high absorption coefficient nature of CdTe enables it to be especially suitable for producing thin-film solar cells. However, the toxicity and rarity of materials have limited the researching and manufacturing growth of the CdTe and CIGS solar cells.

1.4 Third-generation solar cells: emerging techniques

Aiming to improve commercially-available solar cells by alternating and combining the advantages of previously used technique, the third-generation solar cells are still of laboratory researching. By utilizing previously researched materials and thin-film deposition method, the third-generation photovoltaics aim to produce low-cost, flexible solar cells. They are considered as having the potential to overcome the Shockley-Queisser limit of 30% power conversion efficiency [29] by frequency conversion, hot-carrier effects and multiple-carrier ejection techniques. The emerging technologies include: Copper Zin Tin Sulfide (CZTS), dye-sensitized, perovskite, organic, quantum dot and tandem. [30] [31] The laboratory proved efficiency are summarized in 1-7.

CZTS and CZTSe

Copper zinc tin sulfide (CZTS) and Copper zinc tin selenide (CZTSe) are materials with similar optical and electronic properties to CIGS (discussed in Section 1.3.2) but composed of earth-abundant and non-toxic elements. They have reached certified efficiency of 11% for CZTS and 12.6% for CZTSe. [32]

Dye-sensitized

It is a low-cost photovoltaic technology based on semiconductors formed between a photo-sensitized anode and an electrolyte. It is also known as the Grazel cell. It has reached certified efficiency of 13.1% in 2018. [27]

Organic solar cell

Organic solar cells utilizes conductive organic polymers and small organic molecules for light absorption and charge transport. Their advantages include light-weight nature, inexpensiveness of fabrication, good flexibility and potential disposability. It reaches efficiency of 17.3% with tandem structured organic cells. [33]

Perovskite solar cell

Often constructed as a hybrid organic-inorganic structure, perovskite structured materials are used as the light-harvesting active layer. It has been growing fast in the past decades, reaching efficiency of 29.15% with silicon-based tandem cells (which exceeds the highest achieved efficiency of single-junction Si cells).

Quantum Dot solar cell

Intending to replace bulk materials including Si, CIGS and CdTe, quantum dots have been used as the photon absorbing material to produce low-cost, flexible solar cells. The tunable band-gap property (described in Section 2.2.1) enables the production of multi-junction tandem photovoltaics, where wider range of the solar spectrum could be harvested.

1.5 Quantum Dots Photovoltaics: growing potential

As observed in Figure 1-7, the certified power conversion efficiency of various type quantum dot solar cell has been growing fast in the past decade since 2010, evolved

from lower than 4% to 16.6% in 2019. The rate of growth is not yet slowing down, potentially overcoming the Shockley-Quiesser-limited efficiency of traditional Si-based solar cell.

The main challenge that limits the power conversion efficiency of currently existing devices could be summarized as below:

- absorption: limited by the short diffusion length; could potentially be solved by tandem-structured cells (mentioned in the third-generation solar cell 1.4).
- open-circuit voltage loss, which includes a loss from the Shockley-Queisser limit and a deficit from the existence of the sub-bandgap states (discussed in 2.2.2).

1.6 Previous attempts

In order to passivate the sub-bandgap states remaining on the QD surface (discussed in 2.2.2, several attempts have been made, including annealing PbS/EDT film after spin-coating, synthesizing PbS/X core-shell QDs and performing ligand exchange with inorganic iodide ligands.

1.6.1 Post-annealing method

Multiple studies have reported the performance improvement via air-annealing and reached a consensus that the it is owing to the formation of lead oxide product during the air annealing process.

Zhao *et al*. have reported the use of a two-step processing method consisting of air-annealing PbS/EDT film and post-treating with thiol on PbS QD devices. [34] By annealing the QD layer in air at 110 C for 30 minutes and applying post-annealing treatment with ethanedithiol (EDT) solution, the devices showed improved FF, PCE and V_{oc}, with the sacrifice of decreased J_{sc}. It has been proved to modify the surface properties of the PbS QDs, limiting the interface charge recombination and lowering the current leakage at low applied bias regime.

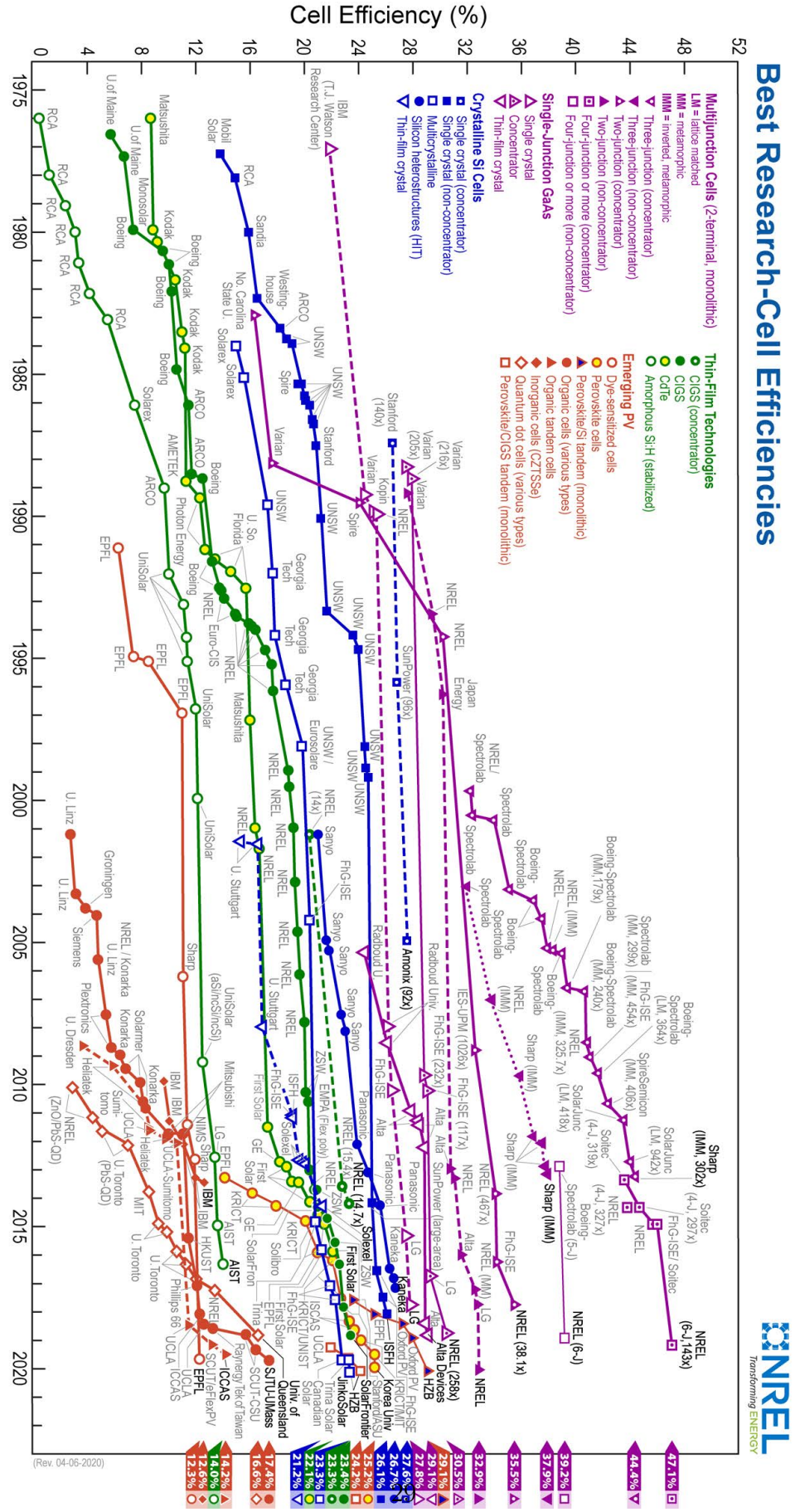

Figure 1-7: Best certified laboratory research cell efficiency chart. Figure from NREL.

Owing to the partial passivation of the oxidation product and the EDT ligands, the device exhibits low J_{sc}, which could be resolved through band-alignment engineering. Chuang *et al*. has reported that the use of EDT and TBAI ligands combined would result in further improvement in surface passivation and continued efficiency improvement [35].

Because of the short-length nature of TBAI ligands, we have seen that PbS QDs with TBAI ligands attached after ligand exchange are not oxidizable, which is problematic in further improving device performances. The pre-anneal method is not applicable in producing tandem solar cells as well, since the post-annealing is achieved via annealing the entire bottom device at 110 C for the PbS layer of the top sub-cells, which brings defects to the bottom organic layers.

1.6.2 PbS/X core-shell QDs

Multiple studies have reported the use of core-shell structured QDs and have seen improved surface passivation via limiting recombination mechanism. Seo *et al*. reported the use of PbS/$CH_3NH_3PbI_3$(MAP) core-shell structured quantum dots on photovoltaics and have seen improved device performances [36]. PbS/CdS (lead sulfide/ cadmium sulfide) core-shell CQD has also been widely discussed regarding the role of surface passivation and improved device performance via the introduction of CdS shell. [37] [38] [39] Neo *et al*. has especially explored the role of surface passivation and the effect of shell thickness and has seen improved open-circuit voltage [37].

1.7 Summary

The urgency of the climate crisis and the historical development of photovoltaic devices has been briefly mentioned in this chapter, reaching a consensus of utilizing solar energy to establish a more sustainable energy future. The three generations of solar cells are introduced, with the discussion of their own advantages and drawbacks. The huge potential of colloidal quantum dots as a competing material for producing the third-generation solar cell has been introduced, leading to the discussion of the

device physics and the feasibility of PbS CQDs.

Chapter 2

Device Physics

In this chapter, the theoretical background necessary to understand this study is explained. Basic photovoltaic principles, including schematics of semiconductors and photon absorption, are described first, and the parameters of evaluating device performances are introduced. The quantum confinement effect of PbS QDs is introduced in this chapter, and the origin of open-circuit voltage deficit - our main challenge in this study - is also discussed.

2.1 Photovoltaics principle

2.1.1 Semiconductor basics

The existing materials could be classified into three categories based on their band-gap (E_g). In solid state physics, the band-gap is defined as the energy difference between the conduction band and the valence band. (Figure 2-1) No electrons are allowed to have energies within the band-gap. In conductors, the conduction band and the valence band overlaps, and thus a large group number electrons are allowed to move and participate in conducting electricity; in insulators, the conduction band and the valence band are so far away that this large band-gap prevent the electrons from being excited to the conduction band and participate in electricity conduction at room temperature. Semiconductors lie between the conductor and the insulator,

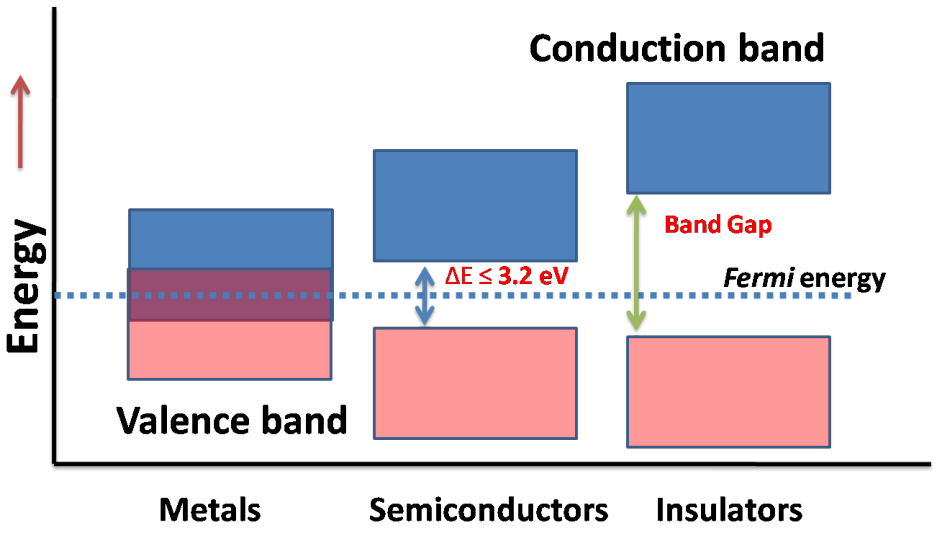

Figure 2-1: Energy band-gap alignment for metals, semiconductors and insulators.

and they have relatively achievable band-gap energy. With sufficient energy applied, electrons are excited to the conduction band and contribute to electricity conduction.

In photovoltaic devices, electrons in the semiconducting materials could be excited from the valence band to the conduction band by absorbing photons with energy equal to or greater than the band-gap, leaving a hole in the valence band. The absence of the electron, or the hole, is considered to be positively charged and could participate in electricity conduction. Since the electrons and the holes carry opposite charges, they are attracted to each other via the Coulomb force. The bounded electron-hole pair is also referred to the exciton. See Figure 2-2 for photon absorption in basic p-n junction solar cell.

2.1.2 Photon absorption

Radiated from the sun through different wavelength and energies with photons, sunlight is filtered through earth's atmosphere and divided into infrared, visible and ultraviolet spectrum. As it passes through the atmosphere, the sunlight is normalized to the shortest path length, which quantifies the reduction in the intensity. The Air

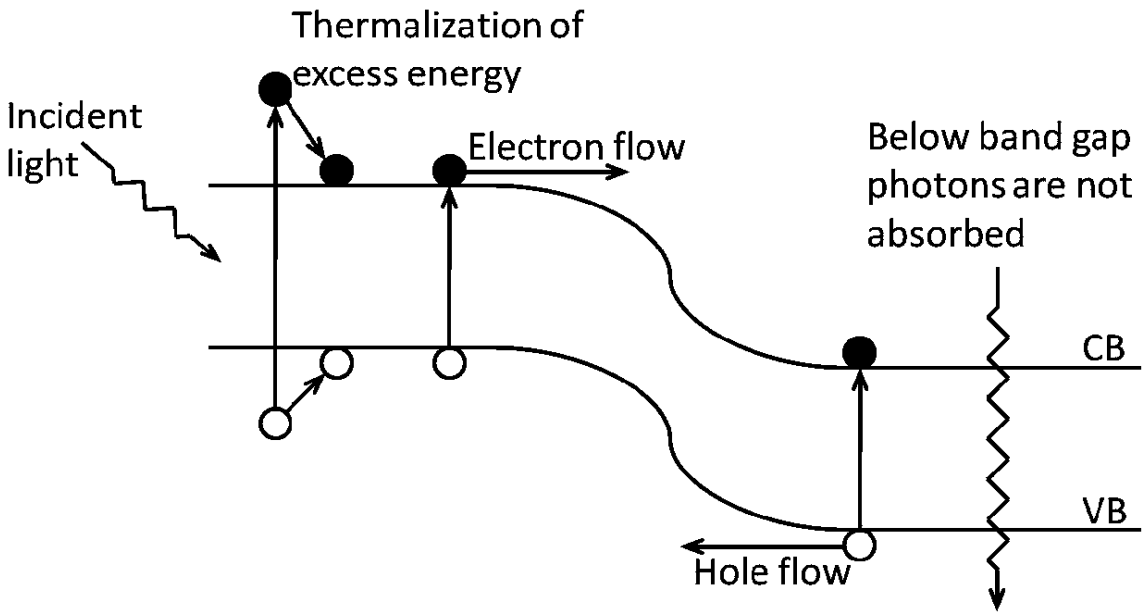

Figure 2-2: Schematic of photon absorption inside basic p-n junction solar cells. VB stands for valence band; CB stands for conduction band. Figure from [8].

Mass quantifies this reduction with the following equation:

$$AM = \frac{1}{cos(\theta)} \tag{2.1}$$

where θ represents the angle between the direct sunlight (shortest path) and the scattered sunlight path. The AM0 spectra refers to directly xabove atmosphere; the AM1 spectra calculates the sunlight from directly overhead and the AM1.5G spectra stands for the conventionally used global solar spectrum for developing photovoltaic devices.

When photons from solar radiation possess an energy higher than the band-gap of the electrons, it gets absorbed with a probability of A_0. Thus, the original intensity of the sunlight experiences a reduction of A_0 due to the absorption over a distance x. It could be calculated by:

$$I(x) = I_0(1 - A_0)^{\frac{x}{4x}} \tag{2.2}$$

in which $x = i \times \triangle x$, and $\triangle x$ is the thickness of the ith layer. Based on the absorption

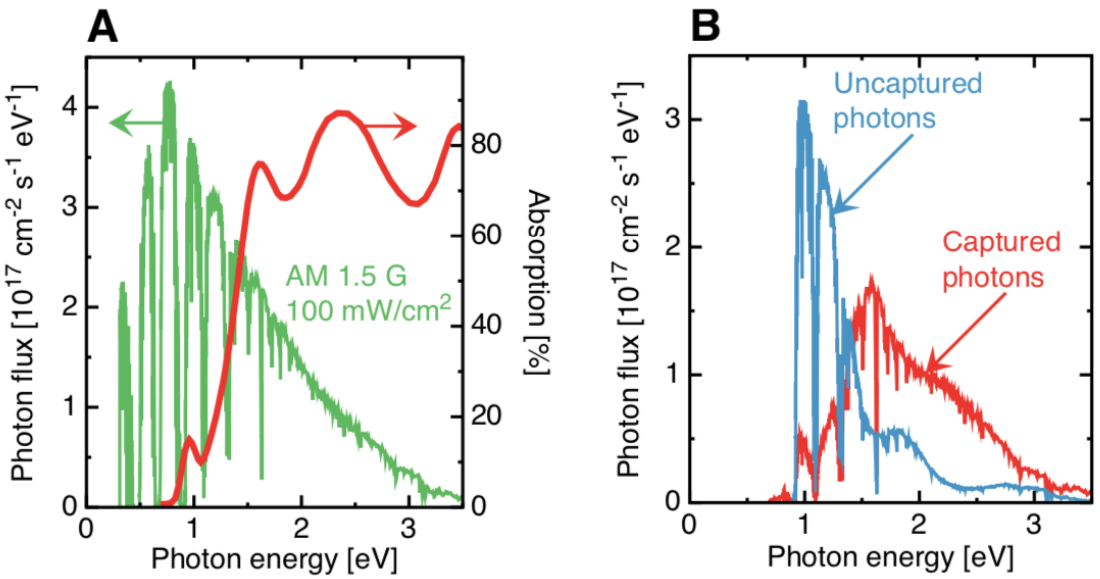

Figure 2-3: (A) Solar spectrum versus photon energy in green and absorption of a typical PbSe (lead selenide) QD device (from [9]) in red. (B) Captured photon flux (in red) and leftover uncaptured available photons (in blue). Figure from [10].

coefficient α given by:

$$\alpha = -\frac{ln(1 - A_0)}{\triangle x} \tag{2.3}$$

Eq.2.2 is equivalent to the following equation:

$$I(x) = I_0 e^{\quad x} \tag{2.4}$$

The photon only gets absorbed when the energy is larger than the band-gap of the electrons. When the energy of the incoming photon is smaller than the band-gap, the photon passes through without getting absorbed. In Figure 2-3, the AM1.5G spectra is plotted with typical absorption of PbSe QD device.

2.1.3 Device performance parameters

Open-circuit voltage (V_{oc}) with Shockley-Queisser limit

The open-circuit voltage could be interpreted as the maximum voltage available from a solar cell and it is determined when there is no net current through the device.

While the short-circuit current (J_{sc}) decreases as the band-gap increases, V_{oc} increases with increasing band-gap. Below, the simplified explanation of the calculation for the maximum theoretical V_{oc} follows the description by Alexi C. Arango, 2010 in [40]

When sunlight is shined onto the device, charge carriers are generated with generation rate G, inducing a photocurrent J_{photo}. The photocurrent is dependent on the light intensity I, layer thickness d, and generation rate G.

$$J_{photo}(I) = qG(I)d \tag{2.5}$$

The total current under illumination is defined as the light current J_{light}. J_{photo} is composed of the light and the dark current, yieldng Eq.2.6; while the photocurrent is independent of the bias applied, most photovoltaics devices do produce small amount of current in dark when bias is applied. The open-circuit voltage (V_{oc}) is the voltage that a photovoltaic device induces across itself in order to cancel the photocurrent generation, and it is defined as the point where J_{dark} and J_{light} are equal and opposite. The calculation of V_{oc} could be given by setting Eq.2.6 to 0.

$$J_{light}(I, V) = J_{dark}(V) - J_{photo}(I) \tag{2.6}$$

As surface trap states are passivated, the non-radiative recombination is minimized and the radiative recombination dominates the current flow with

$$R(V) = Bnp \tag{2.7}$$

in which B is defined as the bi-molecular recombination constant, and n and p are carrier concentrations given by:

$$n \simeq N_c e^{\frac{E_c - E_{Fn}}{kT}} \tag{2.8}$$

$$p \simeq N_v e^{\frac{E_{Fp} - E_v}{kT}} \tag{2.9}$$

where N_c and N_v are the effective density states in the conduction and valence band,

E_c and E_v are the energy level, E_{Fn} and E_{Fp} are the quasi Fermi level of electrons and holes, k is the Boltzmann constant, and T is the temperature.

Given that $qV = E_{Fn} - E_{Fp}$ and $K = BN_cN_v$, plugging n and p into Eq.2.7 and solving for V yields:

$$V = \frac{E_g}{q} - \frac{kT}{q} ln(\frac{K}{R}) \tag{2.10}$$

Under illumination, the total current in Eq.2.6 becomes

$$J_{light}(I, V) = qR(V)d - qG_0d - qG(I)d \tag{2.11}$$

in which $G(I)$ is the thermal generation rate and qG_0d is the small amount of current produced by thermally excited carriers in dark under no bias. Solving for the V_{oc} condition (by setting $J_{light} = 0$) yields:

$$R(V_{oc}) = G_0 + G(I) \tag{2.12}$$

Under high illumination intensities where $G(I) \gg G_0$, using $G(I) = Bnp$ and plugging Eq.2.12 into Eq.2.10 reduces the equation for V_{oc} to

$$V_{ocSQ} = \frac{E_g}{q} - \frac{kT}{q} ln(\frac{N_cN_v}{np}) \tag{2.13}$$

At a finite temperature, the magnitude of the second term in Eq.2.13 is assumed to be about 0.3V and Eq.2.13 could be simplified to:

$$V_{ocSQ} = \frac{E_g}{q} - 0.3\text{V} \tag{2.14}$$

This equation gives the calculation of the theoretical maximum voltage of the photovoltaic device, also known as the open-circuit voltage with Shockley-Queisser limit.

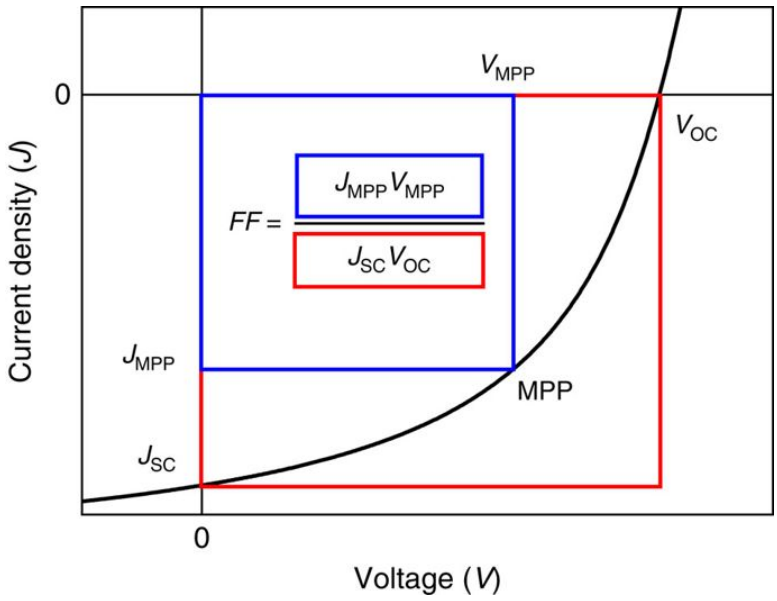

Figure 2-4: Demonstration of FF with $J - V curves$. Figure from [11].

Short-circuit current

The short-circuit current (J_{sc}) is the maximum current generated in a photovoltaic devices and it is defined as the point where the voltage across the device is zero. J_{sc} is dependent on multiple factors, including the surface area and optical properties (absorption and reflection) of the device, light intensity, and the collection probability (which is dependent on the surface passivation and the minority carrier lifetime).

Fill Factor

The fill factor (FF) describes the maximum attainable power of a photovoltaic device. It is defined as:

$$FF = \frac{V_{mpp} J_{mpp}}{V_{OC} J_{sc}} \tag{2.15}$$

in which V_{mpp} and J_{mpp} are the maximum voltage and current density produced by the solar cell. Graphically, FF is the largest rectangle that fits in the $J - V$ curve under illumination. (Figure 2-4)

Power conversion efficiency

The power conversion efficiency (PCE) is determined as the ratio of electrical power produced and the optical power incident on the device, and it is given by:

$$\eta = \frac{Power\ out}{Power\ In} = \frac{V_{mpp} J_{mpp} FF}{Power\ In} \tag{2.16}$$

2.2 PbS CQD properties

2.2.1 Quantum confinement effect

Colloidal Quantum Dot (CQD) is a semiconducting nanocrystalline material with tunable band-gaps. Its size ranges from 2-10 nm in diameter, which guarantees the CQD to be within the quantum confinement regime [41], and the optical and electronic properties of these small particles differ from larger particles. Due to the quantum confinement effect, the band-gap of CQDs increases with decreasing CQD size. This unique property enables CQDs to be synthesizable in different sizes, allowing smaller size dots to suspend in solution and thus being able to be spin-coated. (Figure 2-5) The tunable band-gap also allows the absorption and emission of light in different wavelengths, leading to the use of CQDs in photolvoltaics, LEDs, lasers, etc. [42] [43]

Recently, solution-processed lead sulfide (PbS) CQD has become a competing material for producing low-cost, flexible solar cell due to its tunable band-gap, earth-abundant nature and good stability in air.

The quantum confinement starts to dominate when the size of a semiconductor crystal is smaller than twice the size of its exciton Bohr radius given by:

$$a_B = \epsilon_r (\frac{m_e}{\mu}) a_0 \tag{2.17}$$

in which ϵ_r is the size-dependent dielectric constant of the material, m_e is the mass of the electron, μ is the reduced mass of the exciton and a_0 is the Bohr radius of 0.053 nm. a_B for PbS is approximately 20 nm. [44]

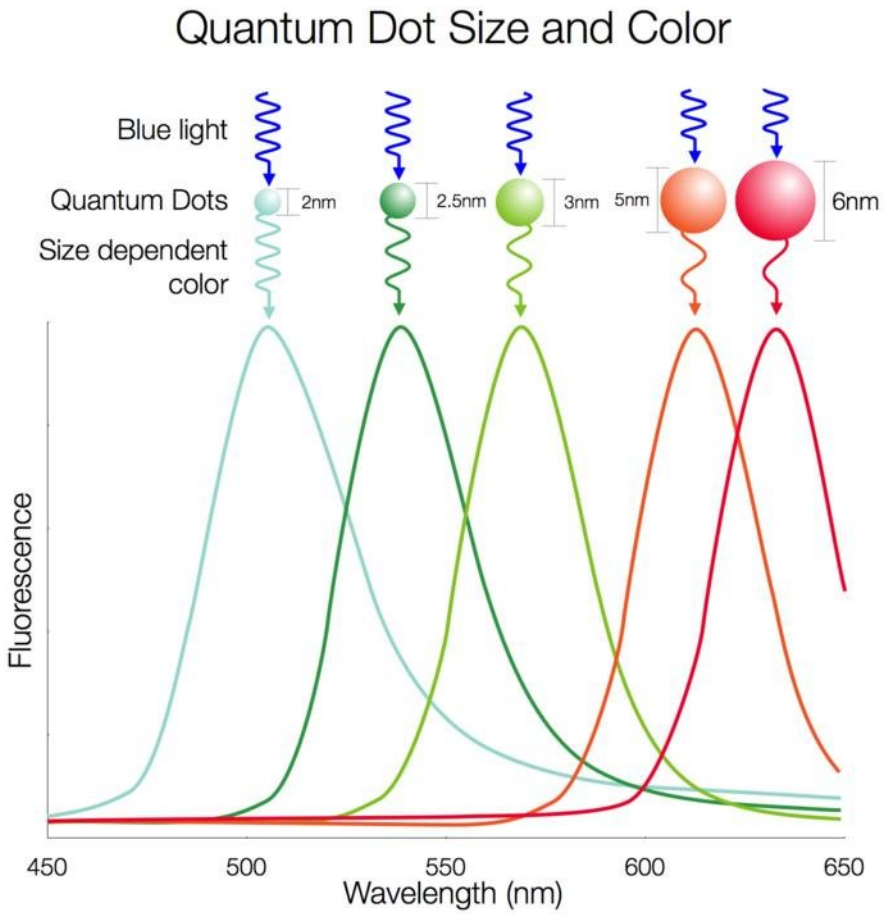

Figure 2-5: Size-dependent nature of CQDs on different wavelength. Figure from [12].

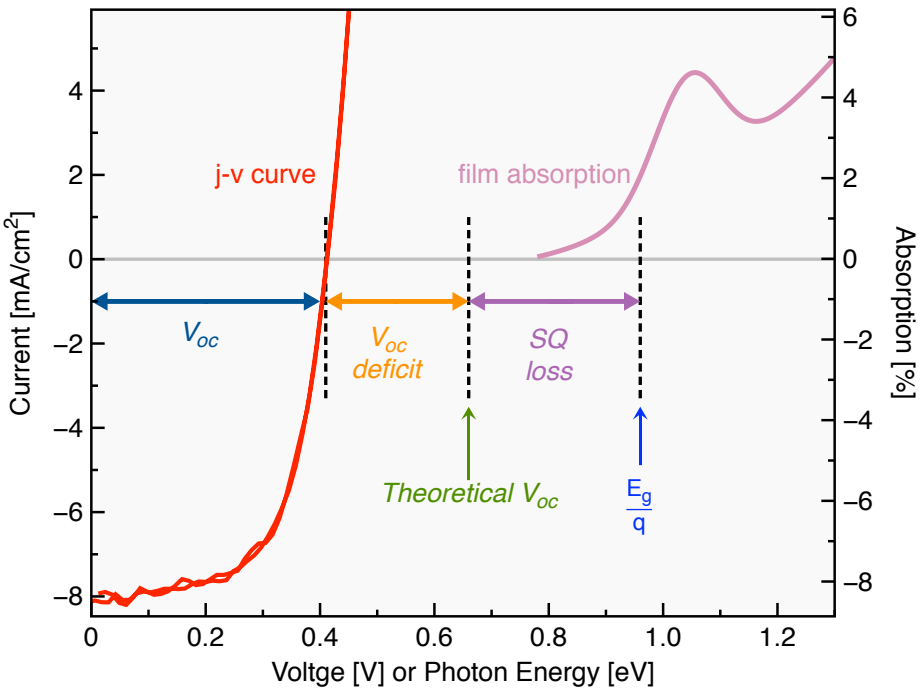

Figure 2-6: Demonstration of V_{oc} deficit with $J-V$ curve (in red) and absorption spectra (in pink). SQ loss abbreviates for Shockley Queisser loss.

The band-gap of PbS QDs is therefore derivable, and is given by [45]:

$$E_g = 0.37 \text{ eV} + \frac{\hbar^2\pi^2}{2r^2}[\frac{1}{m_e} + \frac{1}{m_h}] - \frac{1.8e^2}{17r} + \text{polarization terms} \tag{2.18}$$

in which 0.37 eV is given by the band-gap of bulk PbS, m_e and m_h are the masses of electron and hole, and r is the radius of the PbS QD.

2.2.2 V_{oc} deficit

The theoretical maximum of V_{oc} of photovoltaic devices is given by Eq.2.14. Graphically, the acquired V_{oc} and the V_{ocSQ} could be compared by plotting the $J-V$ curve and the absorption spectra on the same scale (Figure 2-6). Despite of the Shockley-Queisser loss (0.3V) described in Section 2.1.3, most photovoltaic devices are experiencing a V_{oc} loss, which is also observable in our devices in Figure 2-6.

Chuang *et al.* [35] have hypothesized that the main source of V_{oc} deficit is the

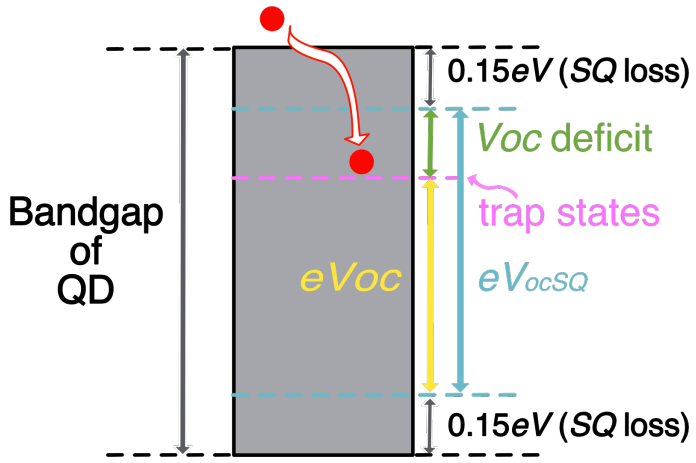

Figure 2-7: Band diagram of PbS QDs with electrons falling into the trap states. The blue lines represent the Shockley-Queisser limit (0.15 eV below the conduction band and above the valence band); the pink line shows the trap-states energy level.

fast carrier recombination rate, which is dominated by the presence of sub-bandgap states, also known as the trap-states. The main limiting mechanism of V_{oc} is depicted in Figure 2-7. The grey area is depicted as the band-gap of the PbS QDs, with the top and bottom dotted lines representing the energy level of the conduction band and valence band, respectively. The two blue lines demonstrate the Shockley-Queisser limit energy level, and the blue arrow represents the maximum achievable V_{oc} times elementary charge, also known as eV_{ocSQ}. Due to the presence of the trap states, the actual acquired V_{oc} is depicted as the energy difference between the lowest trap-states energy level and the S-Q limit energy level, which is demonstrated in yellow. Therefore, the deficit between the acquired V_{oc} and the V_{ocSQ} is clear and depicted in green in the figure.

2.3 Summary

In this chapter, we introduced the basics of semiconducting principles and the device physics of photovoltaic devices. The key parameters of evaluating the device performance of solar cell devices are briefly discussed, and the main limiting mech-

anism: open-circuit voltage deficit, is introduced in detail. We therefore suggest a new method of air-annealing PbS QDs prior to deposition, which is hypothesized to provide better surface passivation and improve device performance via improving open-circuit voltage and deficit.

Chapter 3

Device Fabrication and Characterization

In this chapter, the device structure, solution preparation procedure and device fabrication process are discussed. The detailed procedure of proceeding the innovative pre-anneal method is explained in detail. The device characterization procedures, including absorption measurement, absorbance model fitting and $J-V$ measurement, are also introduced. All devices were fabricated in the Next Generation Photovoltaics Lab at Mount Holyoke College and followed the same fabrication process conducting in an inert nitrogen environment to prevent exposure to oxygen and moisture.

3.1 Device structure

The schematic diagram of our device structure is presented in Figure 3-1 (a). In this PbS QD solar cell shown, the function of each layer is described as below: the ITO-coated glass serves as the front electrode that collects holes with PEDOT on top as an inter-layer that smooth the surface and provide better adhesion; PbS:TBAI layer serves as the photo-active layer, also known as the donor, in which exciton is generated from photon absorption; C60 serves as the transport layer, or the acceptor that accept and transport electrons; BPhen serves as the protection material for bottom layers and Ag (silver) serves as the back electrode that collects electrons. See

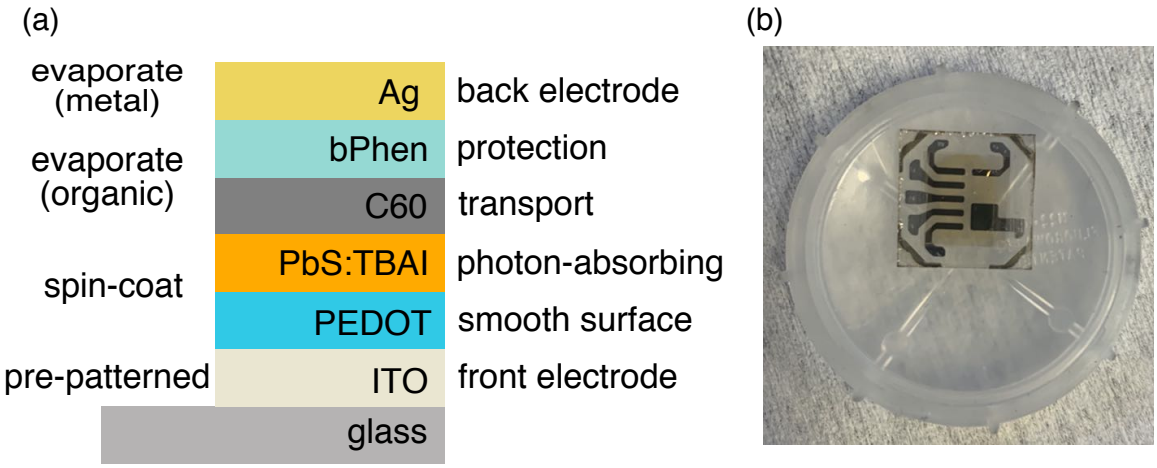

Figure 3-1: (a) Schematic diagram of the structure and function of our devices. (b) As-made device.

Figure 3-1 (b) for as-made PbS QD device.

3.2 Pre-annealed PbS QDs preparation

To prepare the pre-annealed QDs for spin-coating, the Arango Lab follows a uniquely designed procedure from Darcy Wanger's crash-out procedure at MIT in the Bawendi lab to crash-out the PbS QDs in hexane, to anneal the QDs dry in air, and to re-suspend the annealed QDs in hexane for spin-coating.

3.2.1 Preparation

30mL of acetone is prepared through nitrogen bubbling for 15 minutes via a vacuum tubing and schlenk line setting in the chemical fume food. The complete bubbling-off acetone vial is then transferred into the nitrogen glovebox and distribute into smaller vials for further use.

One small vial of butanol, 4 syringes with 22 Gauge needles (labeled PbS, acetone, butanol and hexane), one septum vial labeled chemical waste, and two or four clean empty vials labeled anneal date and time are then transferred into the wet glovebox. The vial cleaning follows the same cleaning procedure described in Section 3.3.1. Size

selection for vials and syringes are dependent on volume of PbS QDs for crash-out.

The amount of solution used is based on the original volume of hexane in PbS QD solution. $\frac{1}{4}$ of the original hexane volume of butanol, and about $\frac{5}{4}$ of the original hexane volume of acetone are added to the PbS QD solution for crash-out. Depending on the amount of butanol and acetone needed, 1.5mL syringe or micro-pipette could be used to control the preciseness of the volume of solution added.

3.2.2 Crash-out

The stock PbS solution is transferred into two clean vials with a clean syringe. Two vials are placed onto the surface of the centrifuge to guarantee that equal amount of PbS solution will be moved into each vial. The amount of butanol based on the amount of hexane in PbS solution, calculated previously, are added into the PbS septum vials via syringe or micro-pipette. The septum vials are capped back immediately after transferring and adding solution to reduce evaporation.

Before adding acetone, the lamp inside the nitrogen glovebox must be turned on and placed in an upright position towards the vials. The acetone is then extracted into the syringe for at least $\frac{3}{2}$ of the original hexane inside the PbS stock solution. The PbS vial needs to be hold uncapped against the lamp with a clear view of solution color, and the syringe needle is placed to be close to the surface of the PbS solution without touching it. Acetone are then slowly added to the vial drop by drop. With each drop of acetone entering the PbS solution, cloudiness is about to form. As the volume of acetone increases, the cloudiness would get fainter and become invisible when the crash-out is complete. When the cloudiness stops forming, the syringe is removed and the mixed solution is capped back immediately and vibrated on the vibrator for 5 seconds.

The same procedure is repeated for two or four times to balance the centrifuge tube. After adding acetone and butanol to all vials, the capped vials are placed into the centrifuge tube. If crashing-out two vials, they need to be placed diagonally instead of adjacently in the centrifuge. See Figure 3-2 (a) for placement of vials in the centrifuge. The amount of solution needs be balanced for centrifugation; if not,

the syringe used to draw PbS solution will be re-used to draw out solution from the unbalanced vial until the two vials equalizes. After the centrifuge tubes are placed correctly and the lid are tightly closed, the centrifugation could be initiated. The rotation speed is set at 4000 rpm with time duration of 3 minutes. To prevent urgent break-down due to unbalanced solution volume, the left hand could be placed on the centrifuge to sense the vibration and the right thumb on the stop button to shut down the centrifuge immediately.

When the centrifugation is complete, post-centrifugation check is neccessary to guarantee a complete crash-out. The PbS vial will be taken out and placed directly under the lamp to check the supernatent color. If the supernatent appears to be close to light tea color, the crash-out is complete; if the supernatent is still dark and cloudy, repeat adding acetone and centrifuging until the color reaches translucent light tea color.

At this stage, aggregations could be observed at the bottom and on the wall of the PbS vial. The supernatent will be viewed as waste and could be poured into the waste vial, leaving the PbS vial uncapped to dry. The vials are placed upside down on a clean TexWipe for left over hexane to drip out; circulation remains off while the nitrogen glovebox remains autopurging during the drying-out process to prevent the impurity entering the uncapped vial. The dry-out procedure takes about 1 hour.

3.2.3 Anneal and re-suspension

While the PbS QDs are in dry-out, the oven has been turned on for pre-heating to ensure that the temperature stabilizes before annealing. After 1 hour of dripping out remaining solution, the PbS QD vial will be wrapped in TexWipe and tin foil, and transferred out from the nitrogen glovebox into the oven for air-annealing. See Figure 3-2 (b) for vials ready to anneal. To allow oxygen to enter the vial, the septum vial is left uncapped in the tin foil wrap with oven door closed to ensure equalized temperature during the annealing process.

After the annealing is complete, the PbS tin foil wrap is transferred into the nitrogen glovebox immediately to prevent moisture from entering the vial. The annealed

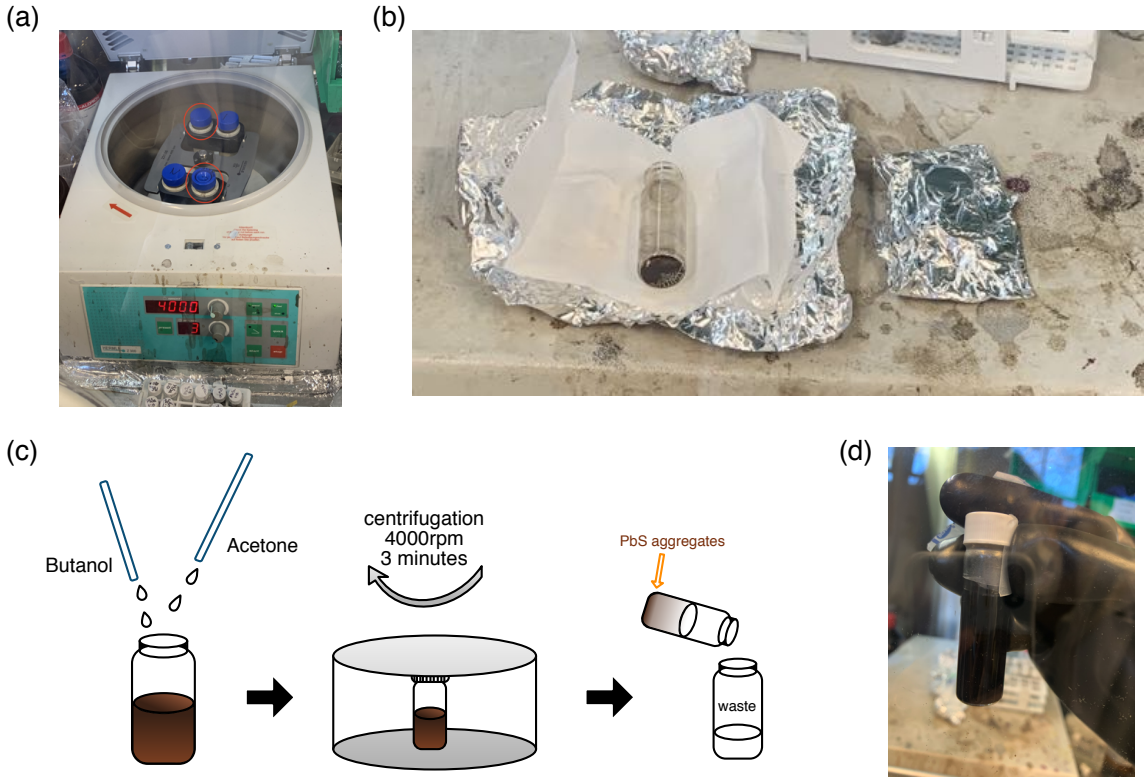

Figure 3-2: (a) Centrifudge tube placement. The circled tubes are for two-vial centrifugation diagonal setting. (b) Crashed-out dry QDs in vial. On the left foil shows the as-crashed-out QDs in uncapped septum vial that is going to be wrapped in TexWipe and tin foil for further annealing; on the right foil wrap it contains the caps that will be stored in wet nitrogen glovebox to prevent contamination. (c) Schematic of crash-out procedure. (d) Re-suspended PbS:hexane solution.

QD vials are left in the glovebox for 30 minutes to allow cooling down. When it returns to the room temperature, re-suspension could be conducted. The annealed QDs could be stored dry in the glovebox to prevent evaporation; if in use, hexane will be added to the dry dots for re-suspension. Depending on the original concentration of stock PbS solution, different volume of hexane could be added into the PbS vial. The vials are capped back immediately to prevent evaporation and change of concentration, and they are vibrated for 5 seconds on the vibrator to ensure full dissolution of QDs in hexane. The new PbS solution is then filtered to remove impurity introduced during crash-out and annealing.

3.3 Fabrication process

3.3.1 Substrate preparation

The indium tin oxide (ITO) patterned glass substrates (Figure 3-3 (e)) are sequentially bathed and ultra-sonicated in Micro-90 solution, de-ionized water, acetone and isopropanol alcohol (IPA) for 5 minutes each: Micro-90 removing greases, water rinsing off Micro-90, acetone reacting and removing organic dirts and IPA washing off residual acetone. The ultra-sonication is performed in the chemical fume hood. The wet ITO substrates are then transferred into the wet nitrogen glovebox and excessive IPA is blown off with nitrogen gun inside the glovebox. The dry substrates are then treated for 60 second in the oxygen plasma to remove greases on the surface and further re-oxidize the ITO surface.

With prepared ITO substrate placing at the center of the high-vacuumed thermal evaporator, 52.5μL of PEDOT:PSS is spin-coated onto the substrate at 3000 rpm for 30 seconds. A thin film of PEDOT:PSS is formed to soften the ITO substrate, creating a smooth surface for the active layers to be deposited. The PEDOT substrate is then placed in high vacuum (10^{-6} Torr) for 30 minutes to allow the excessive moisture from PEDOT:PSS solution to dry out.

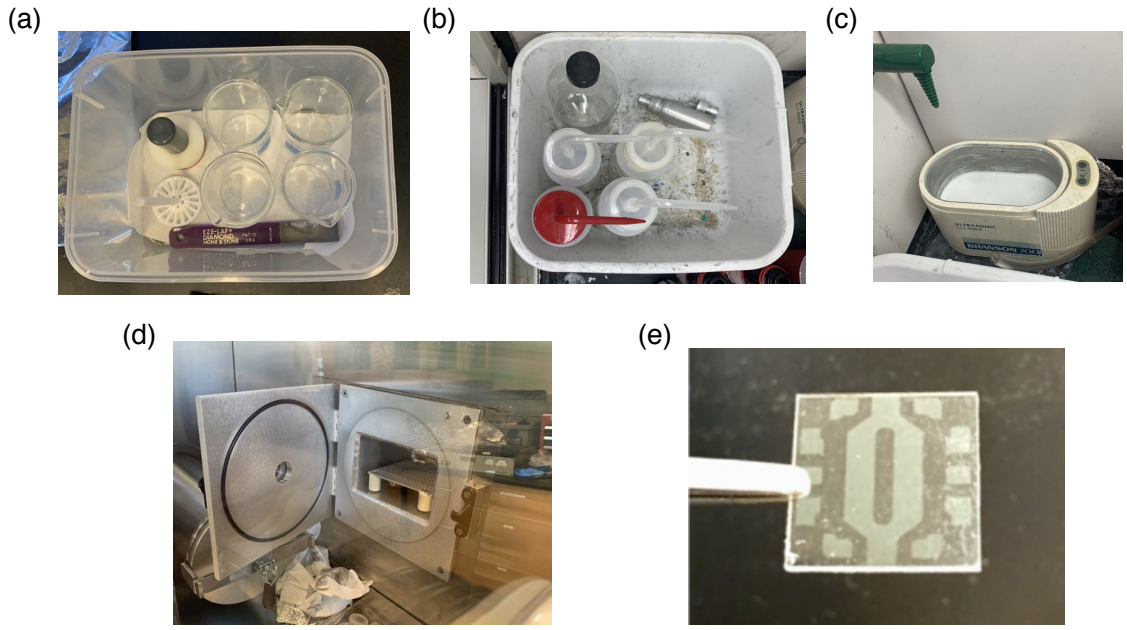

Figure 3-3: (a) Beakers used for substrate cleaning. (b) M-90, acetone, de-ionized water and isopropanol used for cleaning and rinsing. (c) Ultra-sonicator. (d) Oxygen plasma Cleaner. (e) ITO-patterned glass substrate. Figure from [13]

3.3.2 PbS QD layer spin-coating

As-synthesized PbS QDs are capped with oleic acid ligands. As proved in multiple literature, long and bulky oleic acid ligand hinders the mobility of the electrons. To shorten the distance between the QDs, Tetra-butyl-ammonium iodide (TBAI) ligands are used to substitute the oleic acid ligands to provide improved carrier mobility and reasonable energy level alignment. [46] [47] [48] See Figure 3-4 for ligand swap demonstration.

The PbS layer is deposited in the wet nitrogen glovebox. 25μL of PbS QD solution (in hexane) is spin-coated onto the substrate at 2000 rpm for a time duration of 30 seconds. The solid-state ligand exchange is performed in situ with 52.5μL of TBAI solution (1% TBAI in methanol by volume) with the same rotational speed and time duration, and a treatment time of 10 second before spinning is guaranteed with the timer to ensure complete ligand exchange. One methanol wash (52.5μL) is employed to wash out excessive TBAI ligands, with the same rotational speed, time duration

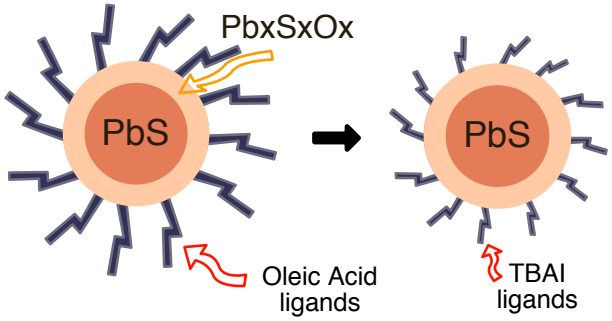

Figure 3-4: Schematic of ligand swap from oleic acid ligands to TBAI ligands.

and treatment time. One extra hexane rinse with no treatment time is applied to rinse out all possible residuals. Four layer-by-layer depositions are employed with the same procedure to build up the PbS film with about 50-80 nm of thickness.

To completely remove the residual moisture, the PbS QD film is stored in the nitrogen glovebox overnight ($\tilde{1}$0 hours) and placed in high-vacuumed thermal evaporator for 1 hour before further deposition.

3.3.3 Thermal evaporation

The organic and metal are deposited by thermal evaporation, a thin-film deposition technique that vaporizes and deposits materials in vacuum. The materials are placed in heat-resistive source boat, and the vaporization temperature is achieved by running high current through the boat. With the substrates being placed facing down in the holder, vaporized materials are deposited directly onto the substrates through the thermal evaporator chamber. High vacuum circumstance (10^{-4} to 10^{-9} Torr) is maintained during the thermal evaporation process to prevent vapor particles from encountering contamination before condensing back to solid state onto the substrates, and it is achieved through a two-stage pump system consisting of a turbo pump and a backing pump. See Figure 3-5 for details of the thermal evaporator.

Prior to preparing the substrates in vacuum in the thermal evaporator, four materials are loaded into the boats: C60 as the acceptor material, BPhen as the protective material and Ag (silver) as the back electrode material. The first three organic ma-

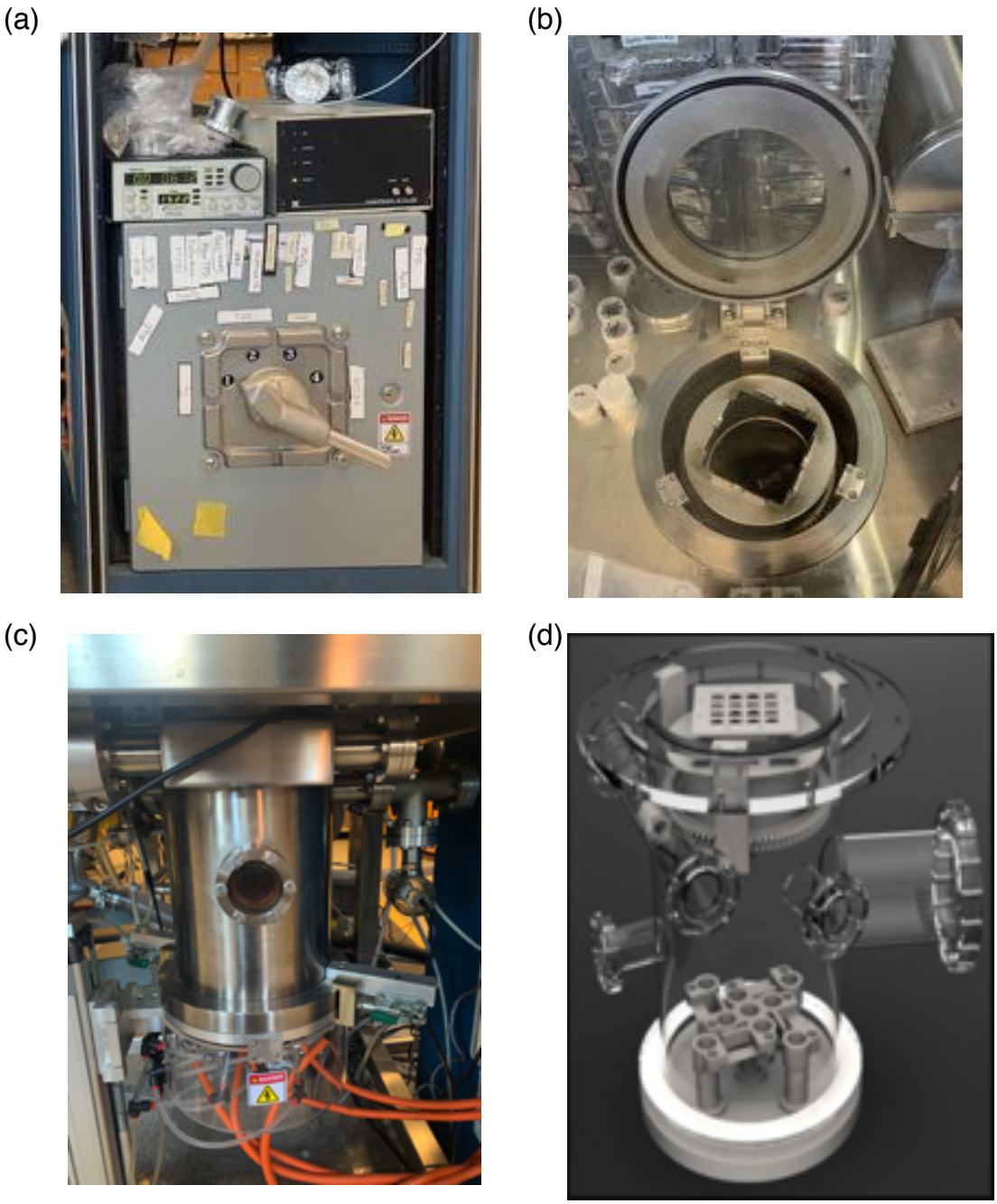

Figure 3-5: (a) Thickness monitor and turbo pump monitor. (b) Top view of thermal evaporator in the nitrogen glovebox. (c) Evaporator chamber. (d) Schematic diagram of the interior design of thermal evaporator. Figure by [14]

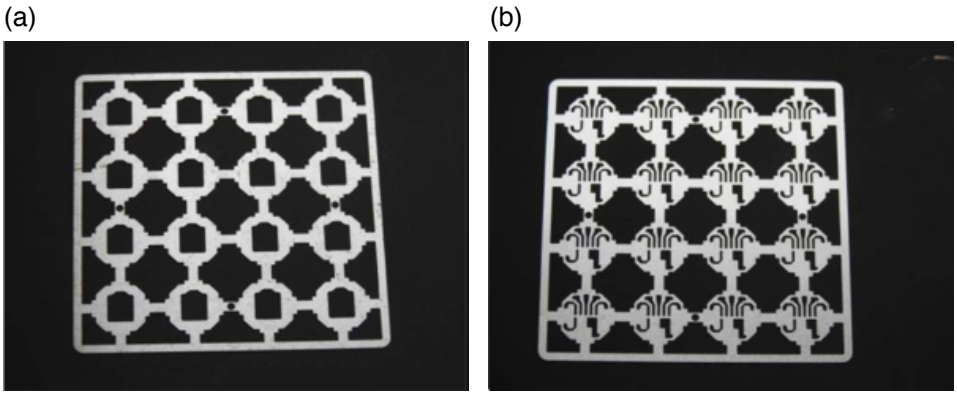

Figure 3-6: Organic (a) and metal (b) used in thermal evaporation. Figure by [14]. Octangular and nine-contact-points Shapes could be observed in Figure 3-1 (b).

terials are deposited using the organic mask, and silver is deposited with the metal mask. See Figure 3-6 for different masks used in thermal evaporation. After carefully loading the substrates, the roughing pump is then used to remove large amount of gas and bring the chamber down to approximately 10^{-5} Torr. The back pump and the turbo pump are turned on in situ to achieve and maintain the chamber pressure at 10^{-7} Torr.

Different deposition rates are controlled through managing the magnitude of applied current, which controls the temperature. Before opening the shutter for deposition, a steady rate of 1-2 $\mathring{A}/s$ is achieved and a waste of 100 $\mathring{A}$ is monitored by the thickness monitor to prevent contaminated particles being accidentally deposited onto the substrates. 40 nm of C60, 7 nm of BPhen and 40 nm of Ag are thermal evaporated sequentially.

3.4 Device characterization

3.4.1 Absorption measurement

The absorption measurements are taken after the spin-coat of PbS layer described in Section 3.3.2. Since the PbS layer is spun on glass substrate with pre-patterned ITO and also contains a bottom layer of PEDOT:PSS, the absorption has already

been taken for the glass substrate and the PEDOT layer for further processing. The FilmTek3000 package from Scientific Computing International is used to performed the optical absorption spectroscopy based on reflection and transmission. This spectrophotometry measurement utilizes a DUV-NIR (Deep Ultraviolet to Near Infrared) fiber-optic spectrophotometer to take the measurement and save as reflection and transmission data. See Figure 3-7 for the spectrophotometry set-up.

A five-oscillator fitting model is used to fit the reflection and transmission data. The model generates the refractive index (N) and extinction coefficient (K) of each wavelength and layer separately (glass substrate, EDT, PbS:TBAI film). The N and K of the PbS layer could then be translated into absorbance with the following equation:

$$\alpha = \frac{4\pi K}{\lambda} \tag{3.1}$$

in which K represents the fitted extinction coefficient with respect to certain wavelength λ.

3.4.2 J-V characterization

After thermal evaporation, the devices are transferred into the dry nitrogen glovebox for current-voltage characterization. The characterization set-up is composed of: a Keithley 2400 sourcemeter to provide voltage input, a xenon lamp solar simulator to provide illumination, and a customized device holder to provide contact points. The Keithley 2400 generates the IV curve with a voltage input from -0.2V to 1.0V. The solar simulator is calibrated to simulate the solar spectrum of AM 1.5G at 25 C with an intensity of 100mW/cm^2. The testing bed consists nine contact points, seven probing the back Ag electrode and two probing the front ITO electro See Figure ... for testing set-up.

The following parameters are extrapolated separately from the J-V curves: J_{sc}, V_{oc}, FF and PCE. The current-voltage data is plotted on a linear scale and a logarithmic scale to present device performances. See Figure 3-8 for demonstration of plots.

(a)

(b)

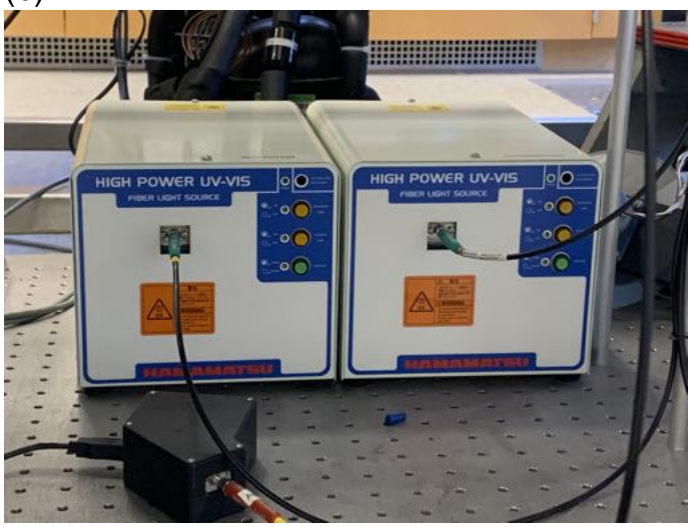

(c)

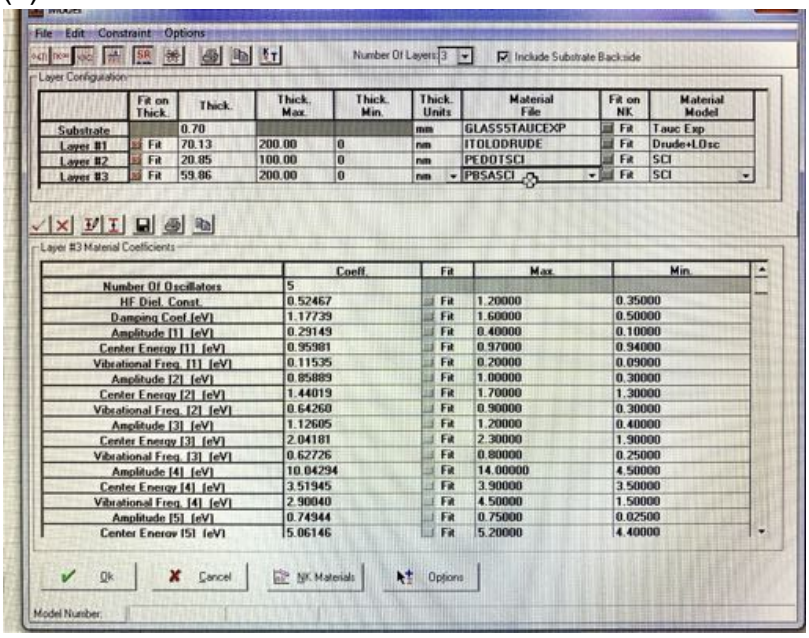

Figure 3-7: (a) Platform for substrate placement of the spectrophotometry set-up. (b) DUV-NIR fiber-optic spectrophotometer. (c) Demonstration of fitting model used for NK data from RT data. 3 layers are fitted separately: the glass substrate layer, the PEDOT layer, and the PbS layer. NK fittings from the PbS layer only would be saved and further processed.

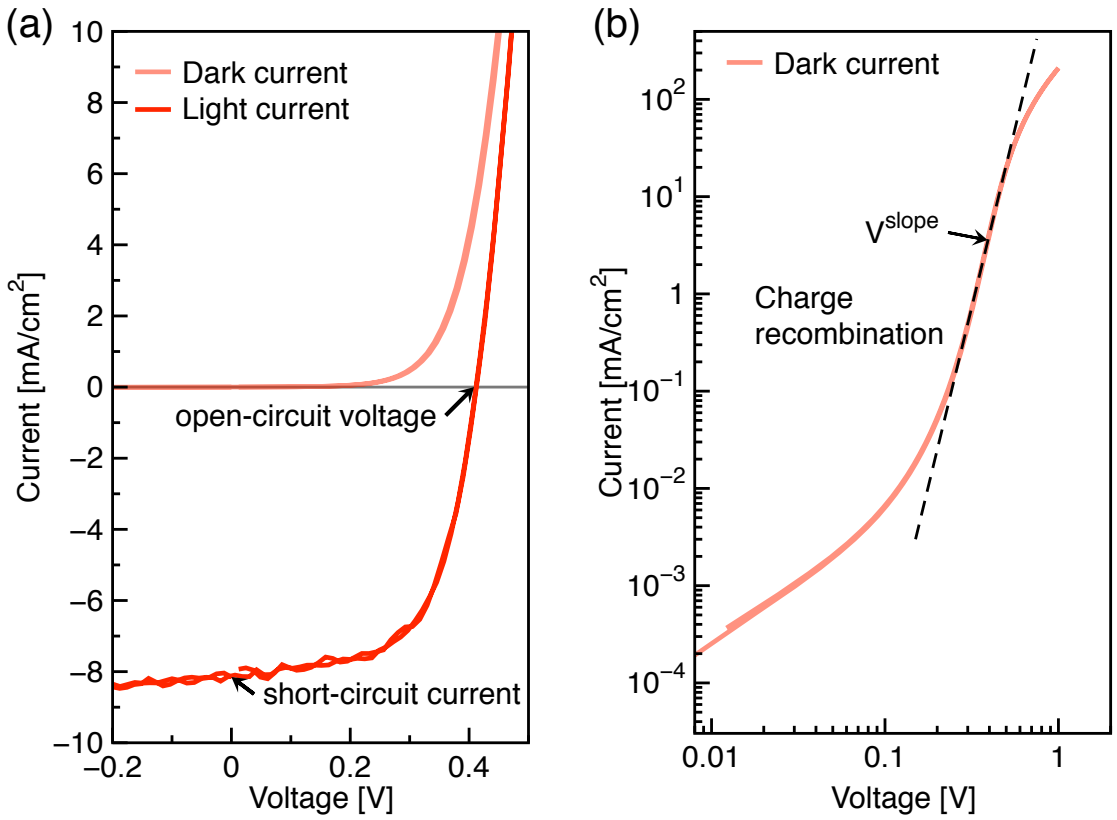

Figure 3-8: Demonstration of light and dark J-V curve on linear (a) and logarithmic (b) scale. The dotted line on the log scale represents the fitting for the recombination region.

Chapter 4

Results

In this chapter, results obtained through X-ray photo-electron spectroscopy, spectrophotometry and current-voltage characterization are presented. Five devices spin-coated with as-synthesized and annealed (1.5hr, 3hr, 5hr and 8hr) QDs are included. The device performances are evaluated through characteristics including: open-circuit voltage (V_{oc}), short-circuit current (J_{sc}), V_{oc} deficit, normalized J_{sc}, Fill Factor (FF) and power conversion efficiency (PCE), which are summarized in Table 4.1.

4.1 X-ray photoelectron spectroscopy spectra

X-ray photoelectron spectroscopy (XPS) was carried out on devices spin-coated with as-synthesized QDs and 3hr annealed QDs to investigate the composition change. The atomic concentration ratio of each element is given in Table 4.2. The presence of lead (Pb), sulfur (S), oxygen (O), and carbon (C) is detected in both films. The carbon originates from the Tetrabutylammonium Iodide (TBAI) ligand. The oxygen component in as-synthesized QD film is likely due to the impurity introduced during the PbS synthesis stage and the air exposure while transferring devices for XPS measurement. The annealed QDs have higher concentration of oxygen, as expected, while the concentration of lead and sulfur decreases due to the introduction of ambient oxygen atoms. The carbon concentration does not widely fluctuate, indicating that the annealed QD has similar concentration of TBAI attached to the surface. About

Table 4.1: Device characteristics for devices spin-coated with as-synthesized and pre-annealed QDs

anneal time	V_{oc} [V]	J_{sc} [mA/cm^2]	normalized J_{sc} [%]	V_{oc} deficit [V]	E_g [eV]	peak width [eV]	FF	PCE [%]
0	0.361	7.76	58.34	0.276	0.937	0.047	0.418	1.172
1.5	0.372	7.02	53.18	0.273	0.945	0.044	0.512	1.512
3	0.418	8.12	59.27	0.257	0.975	0.040	0.608	2.032
5	0.399	6.88	42.17	0.299	0.998	0.037	0.452	1.243
8	0.408	5.92	41.21	0.295	1.003	0.037	0.417	1.247

Table 4.2: Atomic concentration in the PbS QD films

sample	Carbon [%]	Lead [%]	Oxygen [%]	Sulfur [%]
as-synthesized	70.8	10.8	10.1	8.3
3hr annealed	71.1	8.6	15.8	4.8

20% of the original PbS (from 10.8% to 8.6%) has been converted to lead oxide compound, which indicates a relatively aggressive and complete oxidation.

The XPS spectra of Pb 4f peak are shown in Figure 4-1 for as-synthesized (a) and 3hr annealed QD film (b). Peak fittings are processed to identify the lead species in as-synthesized and annealed QD films. Compared with as-synthesized QDs, a red-shift of 0.5 eV (from 138.1 eV to 137.7 eV) is observed for 3hr QDs, and an extra peak is shown at around 139.5eV, indicating the formation of lead sulfur oxides. At our anneal temperature, the oxidation compound is believed to be lead sulfite ($PbSO_4$) and lead sulfate ($PbSO_3$), in which $PbSO_3$ was introduced as impurities during the PbS synthesis. The excessive peak occurs at higher binding energy, and the Pb:O ratio increases from 1:1 to 1:3 for 3hr annealed film, in agree with the hypothesis. See also Appendix for S 2p and O 1s spectrum.

4.2 Absorption spectra

Figure 4-2 plots the normalized absorption spectra with offsets of QD films spin-coated on glass, ITO and PEDOT. The spectrum of as-synthesized QD film exhibits the first excitonic peak at 1.0315 eV, while the spectra of annealed QD films exhibit the first excitonic peak at 1.0331 eV, 1.055 eV, 1.0725 eV and 1.0784 eV consecutively for 1.5hr, 3hr, 5hr and 8hr films. The optical absorption spectra of as-synthesized and annealed QD films show similar shapes and features, indicating that the light absorption is dominated by the PbS core. It agrees with the XPS result that the oxidation does not corrode entirely into the center of the PbS core and the unique quantum confinement and semi-conducting characteristic of PbS QDs are reserved.

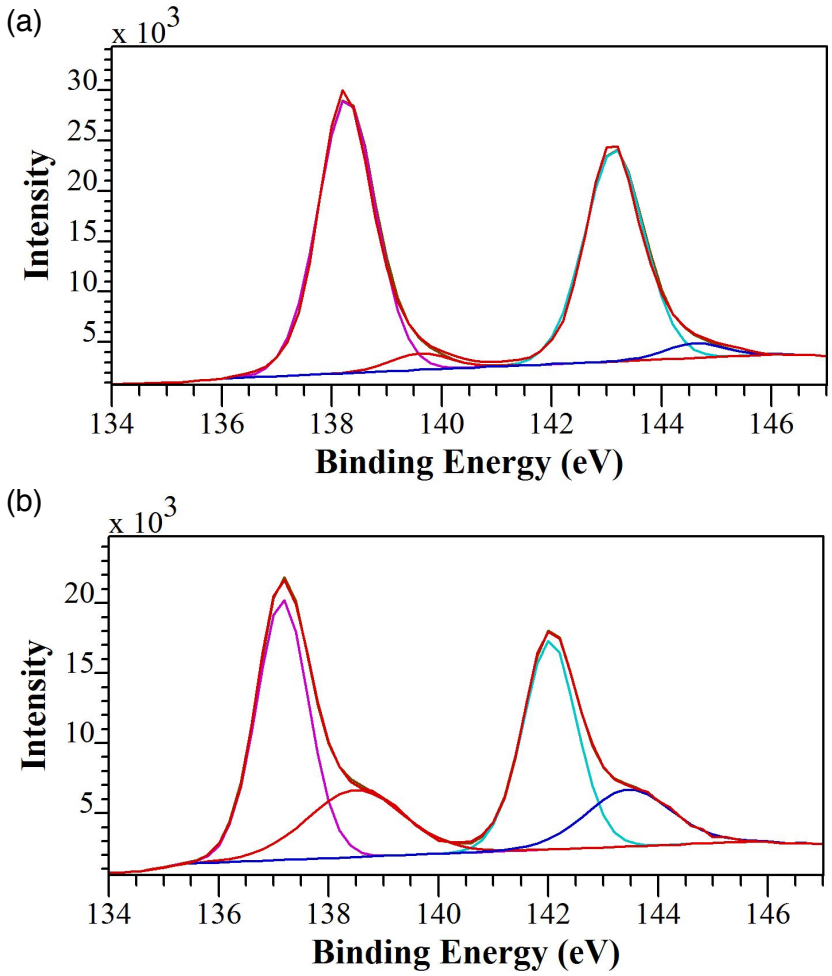

Figure 4-1: XPS spectra of Pb 4f peak for as-synthesized QD film (a) and 3hr annealed QD film (b). The binding energies for the lead compound at Pb 4f region are: 138 eV for PbS, 139.7 eV for $PbSO_4$, 138.8 eV for $PbSO_3$, and 137.9 eV for PbO.

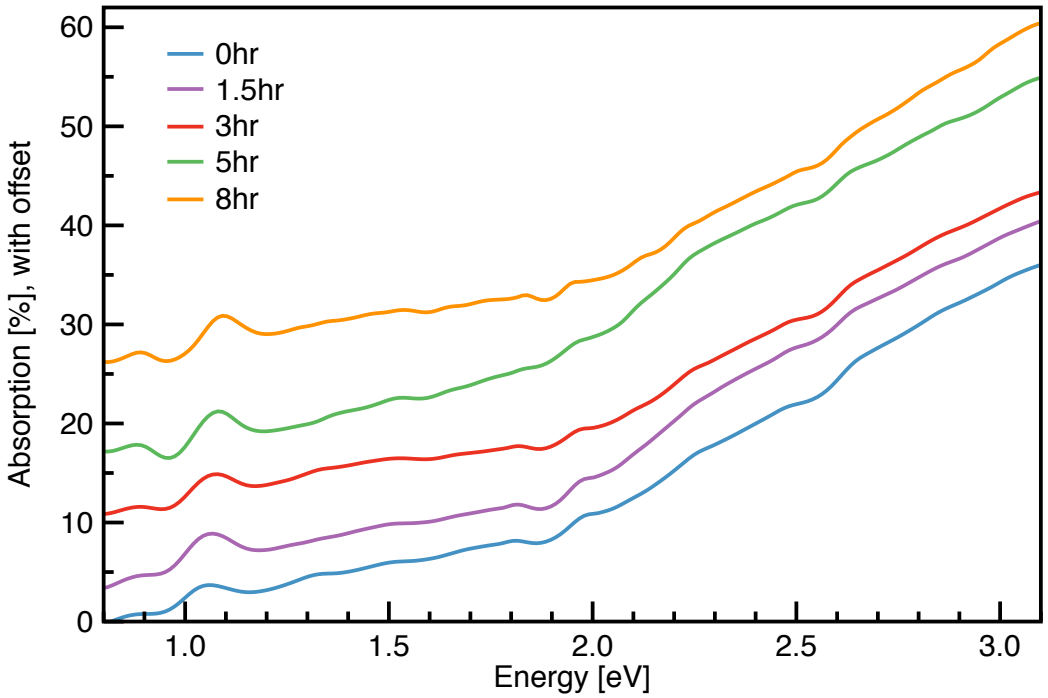

Figure 4-2: Absorption spectra with offsets of as-synthesized and annealed QD films. Absorption is based on transmission and reflection and calculated by: 100% - transmission [%] - reflection [%].

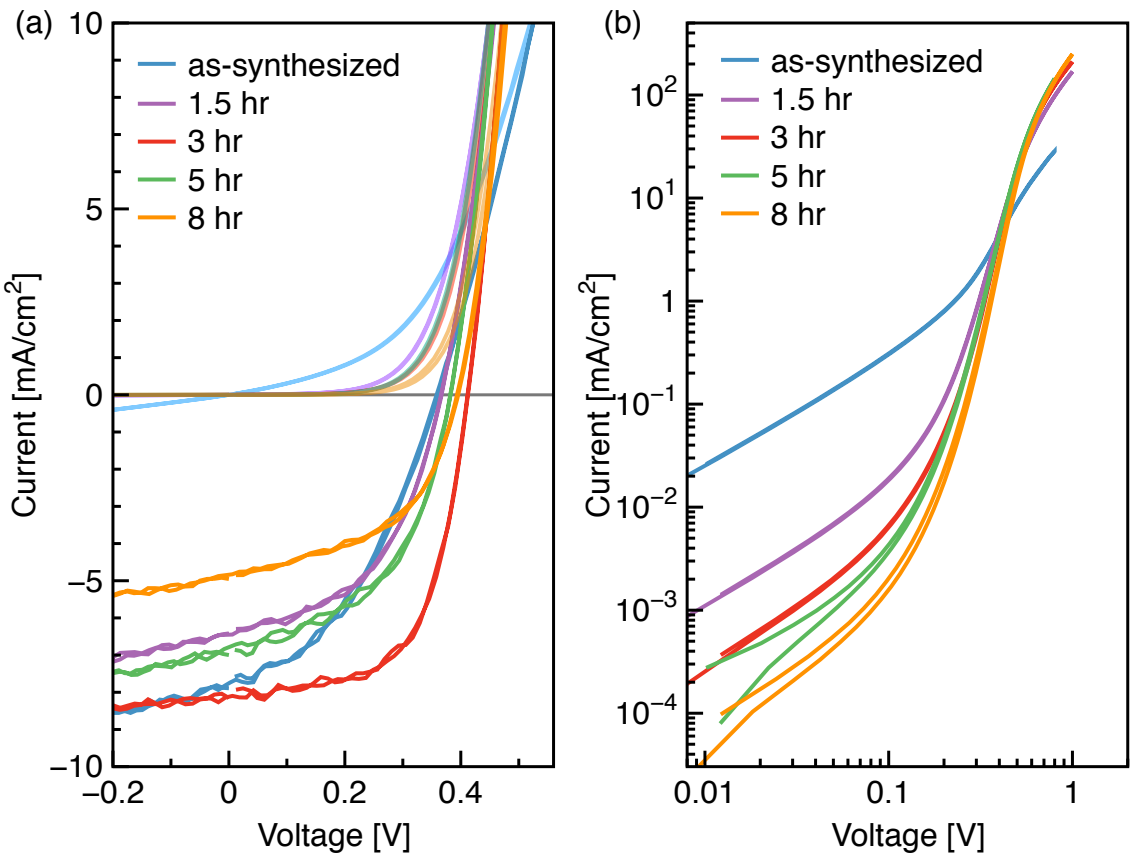

Figure 4-3: (a)Light and dark (semi-transparent) J-V curves of the as-synthesized (in blue) and pre-annealed 1.5hr (in purple), 3hr (in red), 5hr (in green) and 8hr (in orange) devices in linear scale. (b) Dark J-V curves under forward bias on a logarithmic scale.

4.3 J-V characteristics

Figure 4-3 presents the J-V curves of as-synthesized and annealed devices on linear and logarithmic scales. From the linear plot, we observe an increase in V_{oc} from as-synthesized to 1.5hr, 3hr, 5hr and 8hr consecutively, with an improvement of 0.057V at most, about 16% increase from as-synthesized device. Unsurprisingly, the V_{oc} increase is achieved through sacrificing the J_{sc}, which experiences a reduction of 1.84 mA/cm^2 at most, from 7.76 mA/cm^2 (as-synthesized) to 5.92 mA/cm^2 (8hr), about 24% reduction. The 3-hr device achieves the best overall device performance, which is observable from Figure 4-3 (a), with the highest V_{oc} (0.418V) and highest

J_{sc} (8.12 mA/cm^2). The highest FF measures 0.608 for the 3hr device, about 145% of the FF of as-synthesized device (0.418). The power conversion efficiency is also peaked at 3hr device (2.032%), with an increase of 73% compared with as-synthesized device (1.172%).

At low applied bias regime, we observe from the logarithmic J-V curve in dark (4-3 (b)) that much higher leakage is observed for as-synthesized device compared with annealed devices. Longer anneal time leads to lower leakage by a magnitude of 10 from as-synthesized to 1.5hr and 3hr devices, and the improvement in leakage current slows down when the anneal time exceeds 3 hour. All curves exhibit similar transition to the space-charge limit current with high applied bias, but annealed devices attain higher current at high applied bias regime, and only as-synthesized device exhibits a suppression in forward bias current. Annealed device also show increasingly steeper slope in the trap-filling space charge limit current regime with increasing anneal time, observed as an increase in power law during the charge recombination.

Chapter 5

Discussion

In this chapter, the evaluation of the function and performance of as-synthesized and annealed devices are provided. An optimization of the anneal time are given based on the device characteristics, mostly on the trade-off between open-circuit voltage (V_{oc}) and short-circuit current (J_{sc}), and also on V_{oc} deficit. The J-V curves in dark are evaluated in detail to investigate the optimized anneal time and shell thickness. A hypothesis based on band-gap and trap states will be introduced to explain the improvement in device characteristics and to search for optimization.

5.1 Peak information: oxidation and composition change

Figure 5-1 shows the absorbance spectra based on NK data processed in Section 3.4.1. The absorbance spectra is fitted using a Fermi-Direc function and a Gaussian function:

$$\alpha = A_0 + A_1 e^{\frac{(E - E_\mu)^2}{2\sigma^2}} + \frac{A_2}{e^{\frac{(E - E_\mu)}{A_3}} + 1} \tag{5.1}$$

in which E is the location of the first excitonic peak and σ corresponds to the width of the peak. The peak width describes the uniformity of PbS size distribution; the lower the peak width, the closer the size distribution of PbS core.

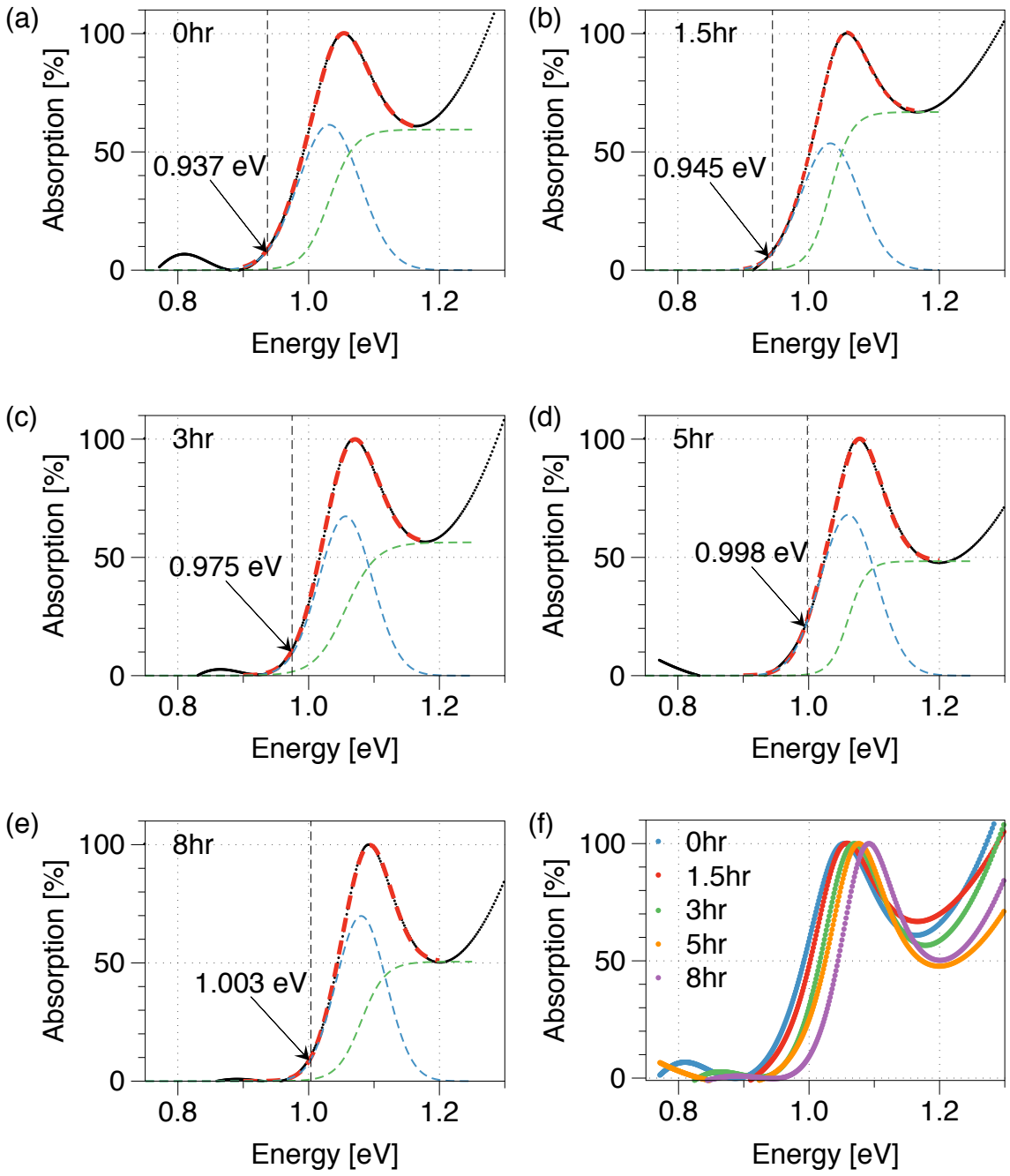

Figure 5-1: Absorbance (in black) calculated from NK and fitting function (in red) applied to absorbance for as-synthesized (a), 1.5hr (b), 3hr (c), 5hr (d), 8hr (e) and all films (f). The Gaussian function and the Fermi-Direc function applied in the fitting are shown in the plot as green and blue dotted lines.

The band-gap E_g of the PbS QDs is given by the following equation:

$$E_g = E \ - 2\sigma \tag{5.2}$$

Figure 5-2 (a) plots E_g vs. σ with increasing anneal time. As-synthesized QDs are measured $E_g = 0.94$ eV and $\sigma = 0.047$ eV, while the 8hr annealed QDs are measured $E_g = 1.0$ eV and $\sigma = 0.037$ eV. The trends of the band-gap and peak width could be described by the Fermi-Direc function. The trend of decreasing band-gap is similar to what Sadovnikov et al. [49] has observed for percent PbS content with increasing anneal temperature.

The radius of PbS CQD is estimated with an empirical relationship between its size and band-gap, proposed by Moreels et al. [50]:

$$E_g = 0.41 + \frac{1}{0.1r^2 + 0.0566r} \tag{5.3}$$

where E_g is the measured band-gap and r is the radius of the PbS core. When annealed in air, the outer surface of PbS QD experiences an oxidation process, forming an oxide shell consisting of lead sulfur oxides. Given that the overall counts detected in XPS measurement does not vary tremendously from as-synthesized to annealed film, we could safely draw the assumption that the overall size of the PbS/$Pb_xS_xO_x$ QDs does not change. Thus, the thickness of the oxide shell is given by:

$$d = r_0 - r \tag{5.4}$$

in which d is the shell thickness in nanometer, r_0 represents the original radius of as-synthesized QDs, and r is the radius of annealed QD core, calculated from Eq.5.3. We could observe a reduction of 0.1 nm in PbS core radius from as-synthesized to annealed 1.5hr, 3hr, 5hr and 8hr QDs each, in agree with the blue-shift of 10 nm in the first excitonic peak. The thickest shell observed is 0.25 nm, slightly thinner than Neo et al. [37] has observed. The fitting function for the distribution of radius and thickness follows the Fermi-Direc distribution as well, with similar trends and behavior

of band-gap and peak width. See Figure 5-2(b) for distributions and fittings.

To explain the behavior of oxide shell with respect to anneal time, we hypothesize that, during the oxidation process, insufficient anneal time allows only partial oxidation on the surface of the QD. Since the oxidation is partial, the probability of enclosing the surface is low, which results in relatively flat increase of the average shell thickness and decrease of the average core radius with a slight increase in E_g and reduction in peak width. With sufficient oxidation time, a complete shell starts to form, reducing the core radius more rapidly. The oxidation is likely to take place via the following reactions:

$$PbS + \frac{3}{2}O_2 = PbSO_3 \tag{5.5}$$

$$PbS + 2O_2 = PbSO_4 \tag{5.6}$$

in which $PbSO_3$ originates from impurity in the synthesis and $PbSO_4$ dominates the oxidation when annealed in air. When the surface passivation is complete, the reduction of PbS size and increase in shell thickness plateau, reaching an equilibrium stage.

5.2 Charge recombination and power law

A power law fit (Figure 5-3) is applied to the charge-recombination region on a logarithmic scale to compare the device performances. The as-synthesized device exhibits a low power law (3.12), while annealed devices show increasing power fit with increasing anneal time. The 1.5hr, 3hr, 5hr and 8hr annealed devices present the power law fit of 6.16, 6.95, 7.36 and 7.72 sequentially, with a increase of 147% increase at most from as-synthesized to annealed devices.

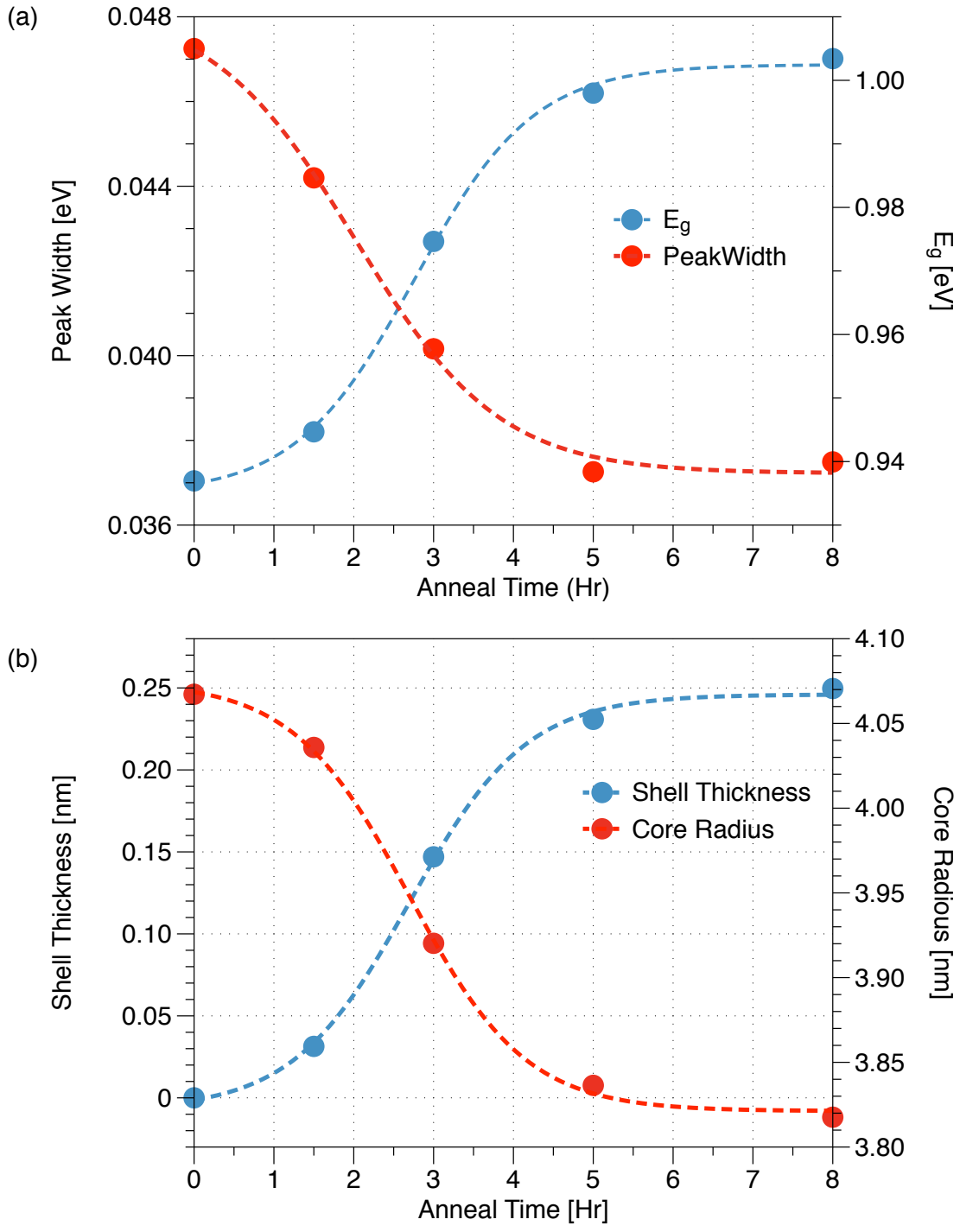

Figure 5-2: Band-gap and peak width (a), and radius and shell thickness (b) with increasing anneal time. The fittings are described by the Fermi-Direc function.

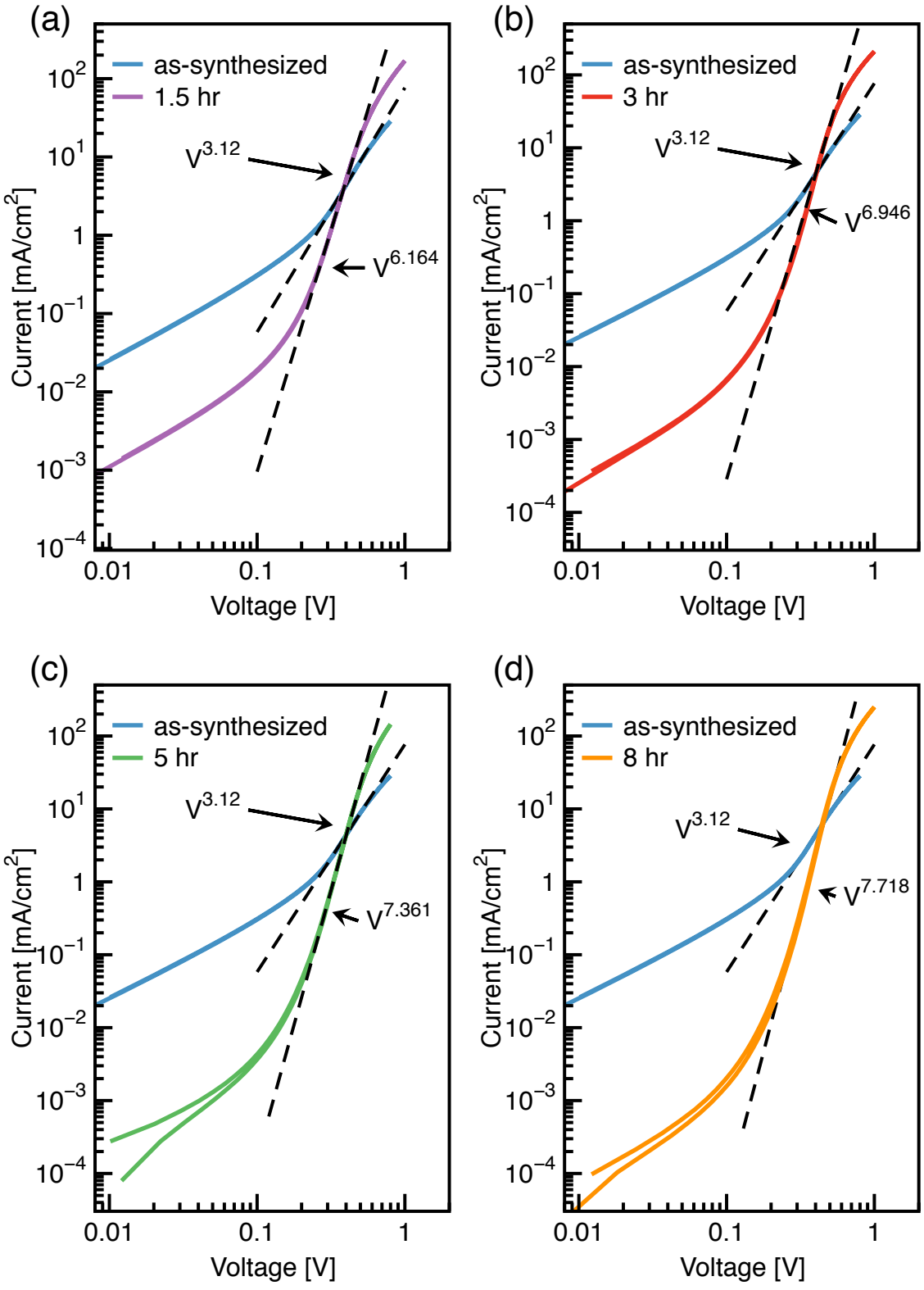

Figure 5-3: Power law fit comparison between as-synthesized and 1.5hr (a), 3hr (b), 5hr (c) and 8hr (d) annealed devices. Fitting is applied to charge recombination region, normally between 0.2V and 0.6V.

5.3 Trade-off and optimization

To provide a clear visualization, V_{oc}, V_{oc} defict, J_{sc}, normalized J_{sc} (J_{sc} normalized by the absorption of each device) are plotted against the double x-axis: E_g and shell thickness to determine the optimized point.

Figure 5-4 plots the V_{ocSQ} (theoretical maximum V_{oc}), V_{oc} and V_{oc} deficit on the double x-axis. The V_{oc} increases steeper than the slope of the V_{ocSQ} increase, which indicates that the increase in V_{oc} is not owing to the band-gap increase only. It also agrees with the decreasing V_{oc} deficit trend. The V_{oc} follows a trend that peaks at $d = 0.15$nm, while the V_{oc} deficit, as a direct reflection of the device deficiency, follows an inverse trend that reaches the minimum at the same point. Thus, here we conclude that when shell thickness equals 0.15 nm, it provides the most efficient improvement to PbS QDs with the size of 8 $\pm$ 0.5 nm.

Figure 5-5 plots the J_{sc} and normalized J_{sc} against the double x-axis. While J_{sc} provides a direct observation of device performances, normalized J_{sc} (J_{sc} over absorption) more precisely evaluates the device characteristics without introducing the effect of the discrepancy in film thickness and absorption. The J_{sc} and normalized J_{sc} follow a similar trends where at the point of $d = 0.15$nm the device show almost no sacrifice of J_{sc}. It suggests an optimized range of shell thickness between 0.1 nm and 0.15 nm. When the thickness exceeds 0.15 nm, steep reduction of J_{sc} and normalized J_{sc} begins to occur, indicating that thicker oxide shell hinders the conductivity of the film.

As explained earlier, in order to investigate the trade-off between V_{oc} and J_{sc}, these two characteristics are taken into consideration together to find the optimized shell thickness. As shown in Figure 5-4 and Figure 5-5, our device exhibit the best overall performance at $d = 0.15$nm, with the highest V_{oc} and J_{sc}. To avoid the error introduced by discrepancy in device and film thicknesses, we also observe that when $d = 0.15nm$, the device achieves the lowest V_{oc} deficit and comparatively low J_{sc} loss. Thus, in this study, shell thickness of 0.15 nm provides us with the best overall improvement.

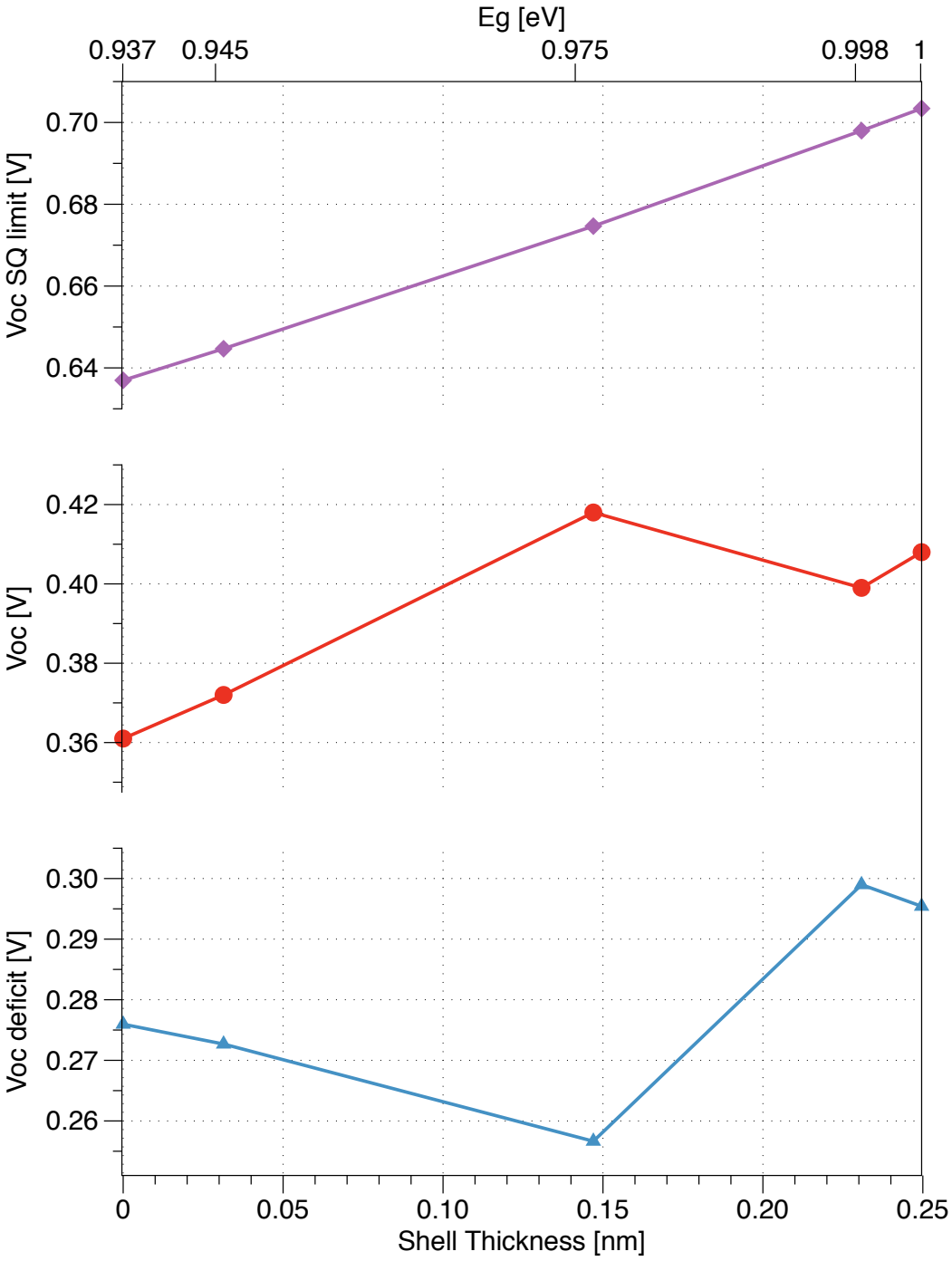

Figure 5-4: Theoretical V_{oc} with Shockley-Queisser limit (in purple), measured V_{oc} (in red) and V_{oc} deficit (in blue) vs. E_g and shell thickness. The top x-axis represents the relative E_g with respect to certain shell thickness

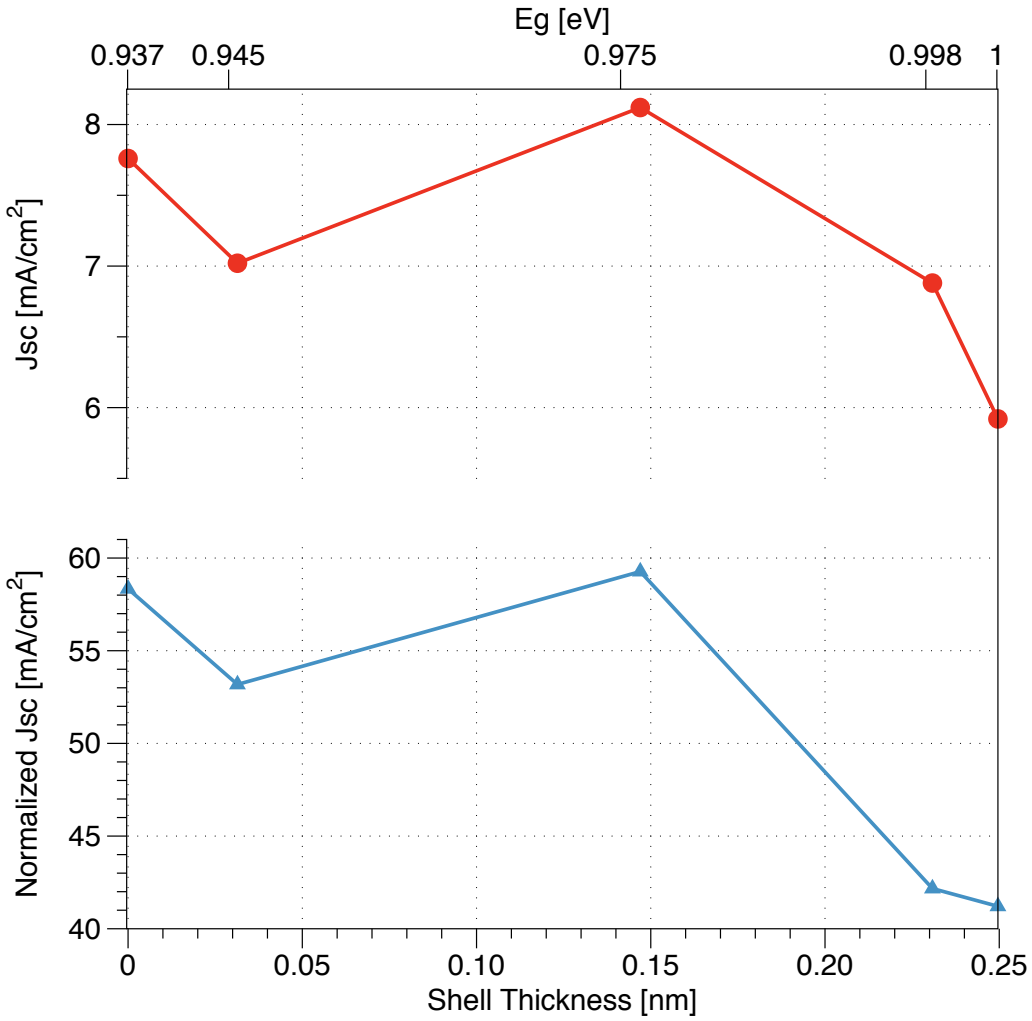

Figure 5-5: J_{sc} (in red) and J_{sc} normalized by film absorption (in blue) vs. E_g and shell thickness. The top x-axis represents the relative E_g with respect to certain shell thickness.

To explain the trends and behaviors shown above, the band-gap and surface trap-states are brought into consideration. Two trap-states are thought to be dominating the device performance: the trap-states on the surface of as-synthesized QDs introduced during the PbS synthesis, and the interface trap-states between the oxides and the PbS core. The surface trap-states of as-synthesized QDs have lower energy level than the interface trap-states, and thus they lead to distinct V_{oc} deficit. With relatively short anneal time, the oxide shell partially closes surface traps while introducing new interface traps, resulting in the co-existence of surface traps and interface traps. Therefore, the V_{oc} deficit is large due to the co-existence of surface and interface trap-states, since the V_{oc} deficit is the discrepancy between the S-Q energy level and the lowest trap-states energy. When the anneal time is sufficient to ensure a complete formation of the oxide shell to enclose the surface trap states, the lowest trap-state energy level moves up to the interface trap, which explains the minimum V_{oc} deficit for an intermediate anneal time of 3hr. As anneal time exceeds optimization, the size of the PbS QDs decreases further, resulting in larger band-gap. However, since the interface trap states remain at the same energy level, the difference between the S-Q barrier and the lowest trap level becomes larger, and therefore resulting in larger V_{oc} deficit. Since the oxide shell also hinders the conductivity of the film, we want to control the anneal time and optimize shell thickness by ensuring that all surface traps are enclosed, while no further growth of oxide shell is produced.

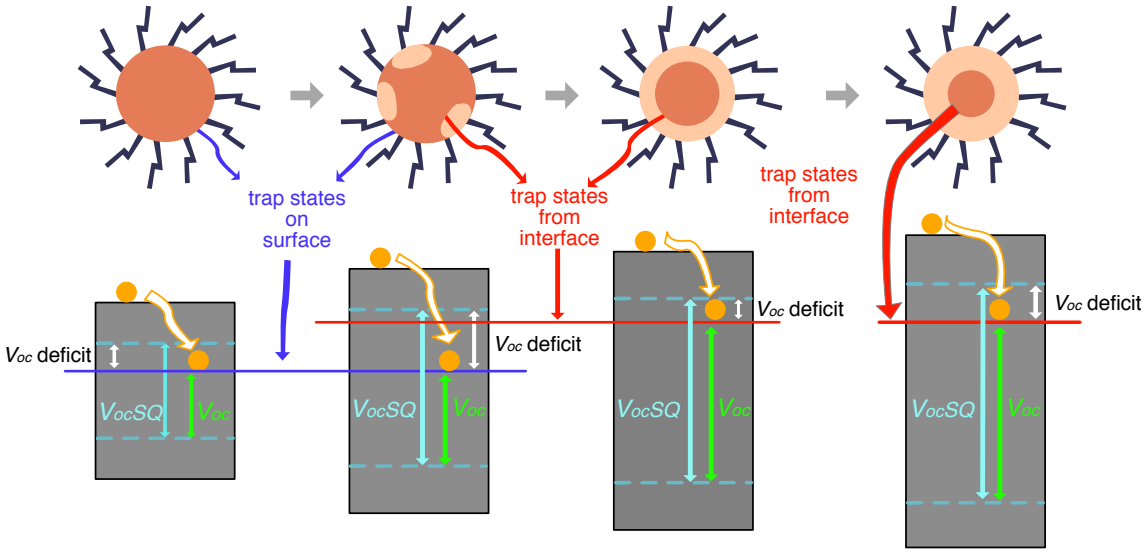

Figure 5-6: Hypothesis of shell growth on PbS QDs capped with oleic acid ligands: from as-synthesized QD to partial oxidation, complete oxidation and over-optimized oxidation.

Chapter 6

Conclusion

In previous chapters, we have designed an innovative pre-annealing method that shells the QDs prior to deposition. Simplified procedure of the pre-annealing method includes: crashing-out as-synthesized PbS QDs capped with oleic acide ligands in the nitrogen glove box; air-annealing dry dots in air in closed oven at 125 C; re-suspending annealed QDs in hexane and filtering acquired solution. We successfully fabricated devices with improved V_{oc}, FF and PCE. We have compared the device performance of cells made of as-synthesized and air-annealed QDs, and through the extracted parameters from the $J-V$ characteristics, we have seen a 16% increase of V_{oc}, 45% improvement of FF and 73% increase of PCE for the best performed device. We also observed an increase in the power law fit of the recombination region from the dark $J-V$ with the new analytic model. This achievement is thought to be originating from the improved surface passivation of the PbS CQDs and thus the reduced non-radiative recombination mechanism. Through the XPS spectra, we also proved that the oxidation could be done on the dry QDs prior to spin-coating and deposition. We also confirmed that the oxide shell thickness could be controlled and optimized through the analyzation of the Fermi-Direc fitting function.

6.1 Future work

6.1.1 Reproduction on multiple sizes QDs

Although we have concluded that $d = 0.15$nm provides the best overall improvement with our devices, it only applies to cases when the original radius of $\simeq 4$ nm (i.e. $E_g \simeq 0.95$eV). Further reproduction and analyzation on PbS QDs of different sizes are essential to generalize our results and optimize the ideal thickness of this pre-anneal method. It is likely that this method is especially suitable on smaller-sized QDs, since when E_g is small enough but not exceeding the quantum confinement limit, the interface energy level might be aligned to be within the SQ limit energy level and thus no longer result in a deficit in V_{oc}

6.1.2 Investigation of the air stability

Multiple studies have reported the improved air-stability of devices made of QDs with better surface passivation. In our study, PbS QDs have been pre-shelled with $PbSO_3$ and $PbSO_4$, and the complete shellness of the dots is supposed to prevent the defect from the oxidation when exposing to air and light. Due to limited time, we have not tested the effect of air-exposure to our devices; it is strongly suggested that further investigation should be done to observe the air-stability of devices spin-coated with pre-annealed QDs.

6.2 Implication

To achieve the goal of breaking the Shockley-Queisser limit of photovoltaic devices, obtaining devices with improved V_{oc} deficit is just the first step. We have hypothesized previously that this pre-annealed QDs could be applied to tandem devices and fully-transparent devices, leading to further applications in solar cell regime.

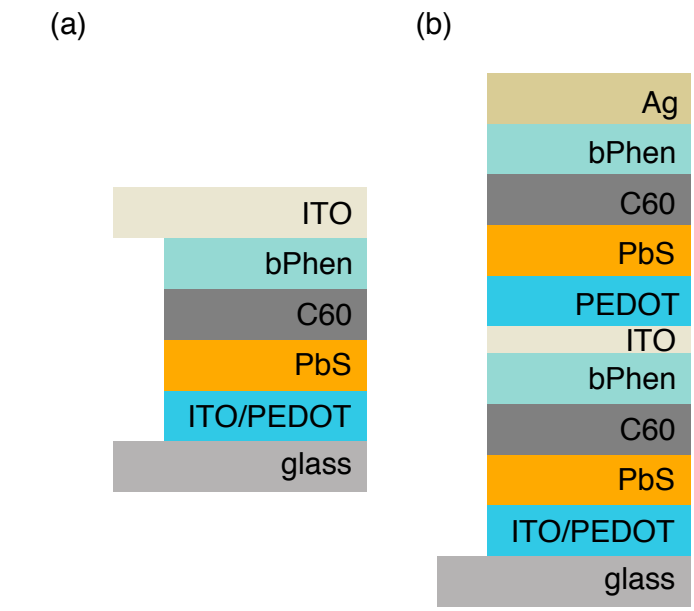

Figure 6-1: Tentative structures of transparent device (a) and two-cell tandem device (b).

6.2.1 Tandem devices

As mentioned in section 1.5, in order to solve the absorption issue limited by the short diffusion length of PbS QDs, tandem-structured cells could be fabricated by stacking sub-cells made of QDs of various band-gap energy levels. With our new pre-annealed QDs, post-annealing bottom cells is no longer necessary to ripen the PbS layers and thus enable the construction of multi-cell tandem structured devices.

6.2.2 Transparent devices

Our study have shown the damage from sputtering ITO as the top electrode when producing fully transparent devices. Although further researching is required to investigate the origins of the damage, we suggest the use of pre-annealed QDs on transparent devices to prevent the damage from the sputtering process.

Appendix A

Sulfur spectra

Here, we present the sulfur figure to assure the formation of oxide compound that encloses the PbS shell. An extra peak of 168 eV is observed for 3hr air-annealed film, which is though to include two species, $PbSO_3$ and $PbSO_4$.

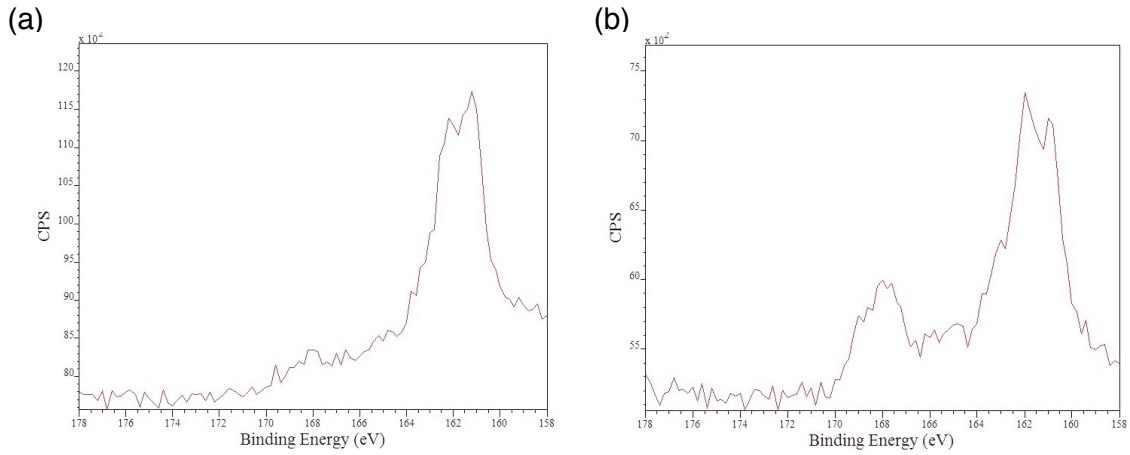

Figure A-1: S 1s spectra of as-synthesized (a) and 3hr air-annealed (b) films.

Appendix B

New analytical model: $J - V$ characteristics in dark on logarithmic scale

An innovative analytic model, adapted from our lab alumna Kathleen Smith, focuses on the $J - V$ curves in dark on the logarithmic scale to analyze and fit each region separately to evaluate our devices. Simplified explanation are adapted from [15]. The model fit of solar cell devices is shown in Figure B-1.

The overall shape of the dark $J - V$ curve is divided into six elements to fit, in which these regions are dominated by different functioning mechanisms. Initially, at low applied bias regime, the linear behavior is dependent on the resistance of the materials, and it is represented as *Resistance* in the figure in red. With higher applied bias, space charges start to build up in the films, which limits the charge injection. It is labeled as *Space Charge*. The fit enters the *Shunting* region when some materials pierce through multiple layers, creating leakage pathway for injected charges. When the applied voltage exceeds the turn-on voltage of the device, the shape follows a power law fit, which indicates the domination from carrier recombination mechanism and is labeled as *Recombination*. The steeper the slope of the power law fit, the better the device performance is. The curve plateaus when the current begins to be limited by the the maximum transport capacity of our material and saturates when entering

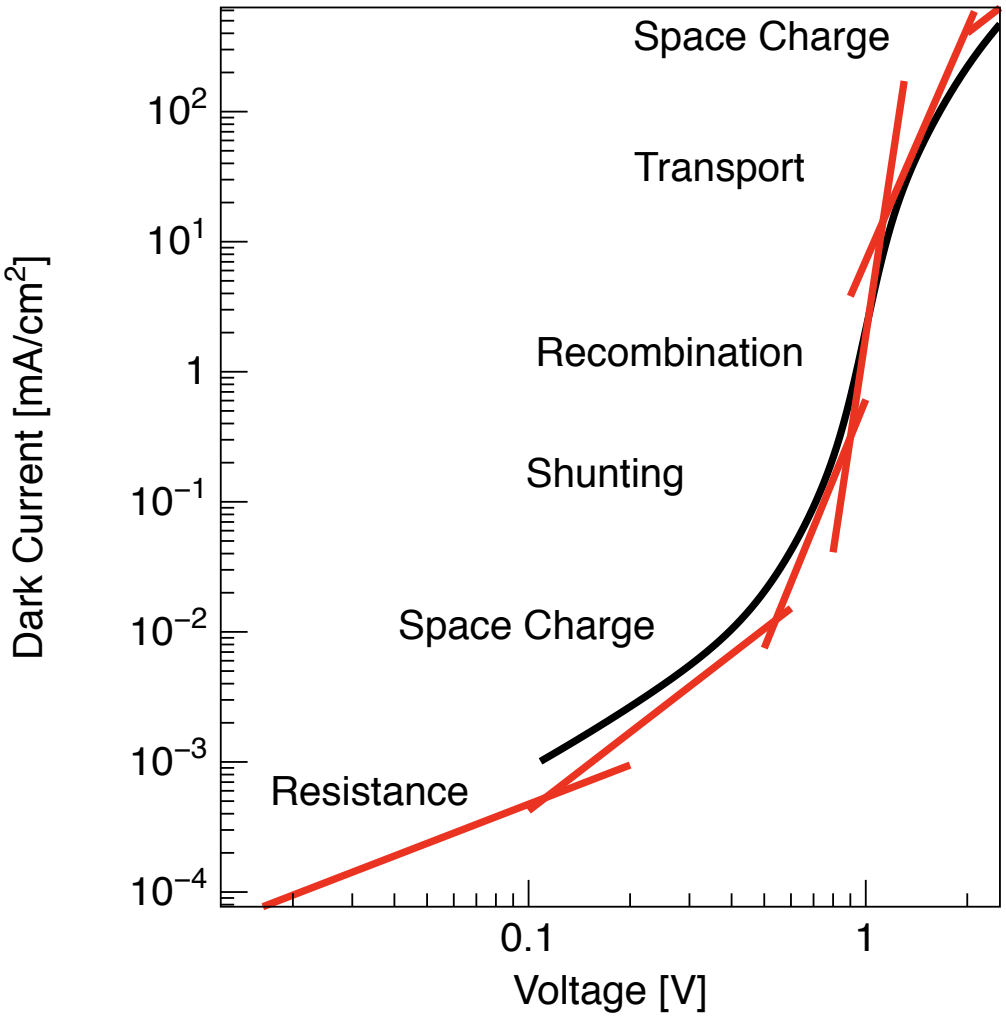

Figure B-1: Model fit of $J - V$ curve in dark on logarithmic scale. Figure from [15].

the space-charge limited regime. It is represented as *Transport* and *Space Charge*.

Bibliography

[1] http://iamtechnical.com/silicon-lattice-doping-silicon-boron-phosporous, title = Silicon Lattice & Doping Silicon With Boron & Phosporous, author = IAMTECHNICAL.com.

[2] PVEducation. A collection of resources for the photovoltaic educator. https://www.pveducation.org.

[3] Jason Svarc. Solar pv cell construction. https://www.cleanenergyreviews.info/blog/solar-pv-cell-construction.

[4] Billy. Photovoltaic – harvesting the power of the sun. https://greensarawak.com/photovoltaic-harvesting-the-power-of-the-sun/.

[5] Tindo Solar. Poly vs mono crystalline. https://www.tindosolar.com.au/learn-more/poly-vs-mono-crystalline/.

[6] D. Lu E. Colegrove J. Moseley C. L. Perkins X. Li R. Mallick W. Zhang R. Malik J. Kephart C.-S. Jiang D. Kuciauskas D. S. Albin M. M. Al-Jassim G. Xiong M. Gloeckler W. K. Metzger, S. Grover.

[7] Wikiwand. Amorphous silicon. https://www.wikiwand.com/en/Amorphous_silicon.

[8] Jeffrey Weisse.

[9] O. E. Semonin, J. M. Luther, S. Choi, H. Y. Chen, J. Gao, A. J. Nozik, and M. C. Beard. Peak external photocurrent quantum efficiency exceeding 100% via meg in a quantum dot solar cell. *Science*, 334(6062), 12 2011.

[10] Alexi C. Arango. Nsf 1704 eager grant proposal for review, 2017.

[11] Davide Bartesaghi, Irene del Carmen Pérez, Juliane Kniepert, Steffen Roland, Mathieu Turbiez, Dieter Neher, and L Jan Anton Koster. Competition between recombination and extraction of free charges determines the fill factor of organic solar cells. *Nature Communications*, 6(1):7083, 2015.

[12] Manu Mitra. Multiple quantum dot tunneling in a semiconductor and its wave function and probability density, 10 2018.

[13] Sue Shi. Tandem colloidal quantum dot solar cells with a novel interconnection design, 2019.

[14] Kathleen Smith. Modelling current-voltage characteristics in organic photovoltaics, 2016.

[15] Kathleen Smith. Modelling current-voltage characteristics in organic photovoltaics, 2018.

[16] EERE. The history of solar. https://www1.eere.energy.gov/solar/pdfs/solar_timeline.pdf.

[17] Solar cooking. http://solarcooking.org/saussure.html.

[18] Beatrice Companies. Bell labs: The solar battery. https://www.beatriceco.com/bti/porticus/bell/belllabs_photovoltaics.html.

[19] Institute for Energy Research. History of solar power. https://www.instituteforenergyresearch.org/renewable/solar/history-of-solar-power/.

[20] John Perlin. Passive solar history. http://californiasolarcenter.org/history-pv/.

[21] Development Solar Energy Research and Demonstration Act of 1974. Public law 93-143.

[22] Alice Buck. A history of the research and development administration. https://www.energy.gov/management/downloads/history-energy-research-and-development-administration.

[23] Department of Energy. History of the u.s. department of energy. https://www.energy.gov/management/office-management/operational-management/history.

[24] Solar Facts and Advice. 3 generations of solar cells. http://www.solar-facts-and-advice.com/solar-cells.html.

[25]

[26] Andrew Sendy. Pros and cons of monocrystalline vs polycrystalline solar panels. https://www.solarreviews.com/blog/pros-and-cons-of-monocrystalline-vs-polycrystalline-solar-panels#advantagesMonocrystalline.

[27] Romain Cariou, Jan Benick, Frank Feldmann, Oliver Höhn, Hubert Hauser, Paul Beutel, Nasser Razek, Markus Wimplinger, Benedikt Bläsi, David Lackner, Martin Hermle, Gerald Siefer, Stefan W Glunz, Andreas W Bett, and Frank Dimroth. Iii–v-on-silicon solar cells reaching 33% photoconversion efficiency in two-terminal configuration. *Nature Energy*, 3(4):326–333, 2018.

[28] GBI Research. Thin-film photovoltaic (pv) cells market analysis to 2020 - cigs (copper indium gallium diselenide) to emerge as the major technology by 2020. http://www.sbdi.co.kr/cart/data/info/2049291778_380dd5fd_GBIAE0010MR_Sample.pdf.

[29] William Shockley and Hans J. Queisser. Detailed balance limit of efficiency of p-n junction solar cells. *Journal of Applied Physics*, 32(3):510–519, 1961.

[30] Gavin Conibeer. Third-generation photovoltaics. *Materials Today*, 10(11):42 – 50, 2007.

[31] Martin Green. Third generation photovoltaics: Ultra-high conversion efficiency at low cost. *Progress in Photovoltaics: Research and Applications*, 9:123 – 135, 03 2001.

[32] PhD thesis.

[33] Lingxian Meng, Yamin Zhang, Xiangjian Wan, Chenxi Li, Xin Zhang, Yanbo Wang, Xin Ke, Zuo Xiao, Liming Ding, Ruoxi Xia, Hin-Lap Yip, Yong Cao, and Yongsheng Chen. Organic and solution-processed tandem solar cells with 17.3% efficiency. *Science*, 361(6407):1094–1098, September 2018.

[34] Ni Zhao, Tim P. Osedach, Liang Yi Chang, Scott M. Geyer, Darcy Wanger, Maddalena T. Binda, Alexi C. Arango, Moungi G. Bawendi, and Vladimir Bulovic. Colloidal PbS quantum dot solar cells with high fill factor. *ACS Nano*, 4(7):3743–3752, 2010.

[35] Chia-Hao Marcus Chuang, Andrea Maurano, Riley E. Brandt, Gyu Weon Hwang, Joel Jean, Tonio Buonassisi, Vladimir Bulović, and Moungi G. Bawendi. Open-circuit voltage deficit, radiative sub-bandgap states, and prospects in quantum dot solar cells. *Nano Letters*, 15(5):3286–3294, 2015. PMID: 25927871.

[36] Gabseok Seo, Jangwon Seo, Seungchan Ryu, Wenping Yin, Tae Kyu Ahn, and Sang Il Seok. Enhancing the Performance of Sensitized Solar Cells with PbS/CH3NH3PbI3 Core/Shell Quantum Dots. *The Journal of Physical Chemistry Letters*, 5(11):2015–2020, jun 2014.

[37] Darren C.J. Neo, Cheng Cheng, Samuel D. Stranks, Simon M. Fairclough, Judy S. Kim, Angus I. Kirkland, Jason M. Smith, Henry J. Snaith, Hazel E. Assender, and Andrew A.R. Watt. Influence of shell thickness and surface passivation on PbS/CdS Core/Shell colloidal quantum dot solar cells. *Chemistry of Materials*, 26(13):4004–4013, 2014.

[38] Arumukham Manjceevan and Jayasundera Bandara. Robust surface passivation of trap sites in pbs q-dots by controlling the thickness of cds layers in pbs/cds

quantum dot solar cells. *Solar Energy Materials and Solar Cells*, 147:157 – 163, 2016.

[39] Belete Atomsa Gonfa, Mee Rahn Kim, Nazar Delegan, Ana C. Tavares, Ricardo Izquierdo, Nianqiang Wu, My Ali El Khakani, and Dongling Ma. Towards high efficiency air-processed near-infrared responsive photovoltaics: bulk heterojunction solar cells based on pbs/cds core–shell quantum dots and tio2 nanorod arrays. *Nanoscale*, 7:10039–10049, 2015.

[40] Alexi C. Arango. PhD thesis.

[41] Stephanie M. Reimann and Matti Manninen. Electronic structure of quantum dots. *Rev. Mod. Phys.*, 74:1283–1342, Nov 2002.

[42] Steven A McDonald, Gerasimos Konstantatos, Shiguo Zhang, Paul W Cyr, Ethan J D Klem, Larissa Levina, and Edward H Sargent. Solution-processed PbS quantum dot infrared photodetectors and photovoltaics. *Nature Materials*, 4(2):138–142, 2005.

[43] D. L. Huffaker, G. Park, Z. Zou, O. B. Shchekin, and D. G. Deppe. 1.3 m room-temperature gaas-based quantum-dot laser. *Applied Physics Letters*, 73(18):2564–2566, 1998.

[44] Chia-Hao Marcus Chuang. *Toward e cient and stable quantum dot solar cells : design and characterization*. PhD thesis, 2016.

[45] L. E. Brus. A simple model for the ionization potential, electron affinity, and aqueous redox potentials of small semiconductor crystallites. *The Journal of Chemical Physics*, 79(11):5566–5571, 1983.

[46] Patrick R. Brown, Donghun Kim, Richard R. Lunt, Ni Zhao, Moungi G. Bawendi, Jeffrey C. Grossman, and Vladimir Bulović. Energy level modification in lead sulfide quantum dot thin films through ligand exchange. *ACS Nano*, 8(6):5863–5872, 2014.

[47] Mengxia Liu, Oleksandr Voznyy, Randy Sabatini, F. Pelayo García de Arquer, Rahim Munir, Ahmed Hesham Balawi, Xinzheng Lan, Fengjia Fan, Grant Walters, Ahmad R. Kirmani, Sjoerd Hoogland, Frédéric Laquai, Aram Amassian, and Edward H. Sargent. Hybrid organic–inorganic inks flatten the energy landscape in colloidal quantum dot solids. *Nature Materials*, 16(2):258–263, 2017.

[48] Xinzheng Lan, Oleksandr Voznyy, Amirreza Kiani, F. Pelayo García de Arquer, Abdullah Saud Abbas, Gi-Hwan Kim, Mengxia Liu, Zhenyu Yang, Grant Walters, Jixian Xu, Mingjian Yuan, Zhijun Ning, Fengjia Fan, Pongsakorn Kanjanaboos, Illan Kramer, David Zhitomirsky, Philip Lee, Alexander Perelgut, Sjoerd Hoogland, and Edward H. Sargent. Passivation using molecular halides increases quantum dot solar cell performance. *Advanced Materials*, 28(2):299–304, 2016.

[49] S. I. Sadovnikov, N. S. Kozhevnikova, and A. A. Rempel. Oxidation of nanocrystalline lead sulfide in air. *Russian Journal of Inorganic Chemistry*, 56(12):1864–1869, 2011.

[50] Iwan Moreels, Karel Lambert, Dries Smeets, David De Muynck, Tom Nollet, José C. Martins, Frank Vanhaecke, André Vantomme, Christophe Delerue, Guy Allan, and Zeger Hens. Size-dependent optical properties of colloidal PbS quantum dots. *ACS Nano*, 3(10):3023–3030, 2009.